science.sciencemag.org/content/367/6483/1235/suppl/DC1

Supplementary Materials for

Persistent influence of obliquity on ice age terminations since the Middle Pleistocene transition

Petra Bajo, Russell N. Drysdale*, Jon D. Woodhead, John C. Hellstrom, David Hodell, Patrizia Ferretti, Antje H. L. Voelker, Giovanni Zanchetta, Teresa Rodrigues, Eric Wolff, Jonathan Tyler, Silvia Frisia, Christoph Spötl, Anthony E. Fallick

*Corresponding author. Email: rnd@unimelb.edu.au

Published 13 March 2020, *Science* **367**, 1235 (2020)
DOI: 10.1126/science.aaw1114

This PDF file includes:

Materials and Methods
Figs. S1 to S8
Tables S1 to S4
References

Materials and Methods

1. Corchia Cave speleothem sampling and stable isotope analyses

Four stalagmites (CC8, CC30, CC119 and CC122) were collected as broken pieces from Galleria delle Stalattiti, a chamber located ~1 km from the tourist entrance of Corchia Cave, Italy (44º 01’ 50” N, 10º 17’ 50” E). Details of the site and chamber characteristics are provided elsewhere (*19, 32-34*). The stalagmites were halved along their vertical growth axis, polished, and then mounted in resin to prevent breaks during subsequent sampling. In section, the stalagmites are white to grey in color and composed of compact translucent to opaque primary calcite devoid of microscopic evidence of either early or late diagenetic alteration. A core sample drilled from a fifth speleothem (CD3), an actively forming subaqueous calcite mound growing in a pool within the same cave gallery (*33, 34*), was also used in this study.

Stable-isotope analyses for each stalagmite were initially conducted at low resolution on powder samples drilled at 1-mm increments along each specimen’s growth axis using a tungsten-carbide dental-drill bit attached to either a Taig CNC micromilling lathe or a Dremel hand drill. Through the portions corresponding to TXII and TX in CC8, micromilling was undertaken at a higher resolution (250 μm) to improve detail. Most of the stable isotope analyses were conducted at the Scottish Universities Environmental Research Centre (East Kilbride, UK), The University of Newcastle (Australia) and The University of Melbourne (Australia) on the same model (AP2003/GV2003) mass spectrometer, each operated in continuous-flow mode. The results are expressed in delta notation relative to the VPDB standard. Long-term analytical precision of in-house reference materials of Carrara marble, previously calibrated to international reference materials NBS-18 and NBS-19, was better than 0.05 and 0.1‰ (1σ) for $\delta^{13}C$ and $\delta^{18}O$ respectively (*23*). Analyses were repeated where $\delta^{18}O$ differed by more than 0.4‰ between adjacent samples. The CD3 core section was microsampled at 200-μm increments using a New Wave Micromill and analysed by continuous-flow IRMS at the Institute of Geology, University of Innsbruck, using a Thermo Fisher Delta^{plus}XL (*35*), on which the long-term analytical uncertainty for $\delta^{18}O$ and $\delta^{13}C$ is 0.08‰ and 0.06‰ respectively (*36*).

2. Corchia Cave speleothem geochronology

Samples for U-Pb dating were extracted at the University of Melbourne using a dental air drill fixed to a manually navigated milling machine. Despite the high U and low common Pb content of these samples (Table S1), their relatively young age required the use of subsamples between 50 and 100 mg to allow for accurate measurement of the radiogenic Pb component. Subsamples were individually immersed briefly in ~0.1M HCl in order to remove potential surface contamination from drilling then thoroughly washed in ultrapure water. All subsequent operations were performed in a multiple-HEPA filtered clean air laboratory. The dried samples were weighed out, dissolved in 6M HCl and spiked with a mixed $^{233}U/^{205}Pb$ tracer solution. Sample-spike equilibration was ensured by overnight heating on a hotplate followed by complete drying down. U and Pb were chemically separated following the ion-exchange procedure (*21*) and isotopic ratios measured on a Nu Instruments Plasma multi-collector-inductively coupled plasma mass spectrometer (MC-ICPMS) at The University of Melbourne. The NIST SRM981 reference material for Pb and an internal $^{238}U/^{235}U$ ratio of 137.88 for U were used for mass-fractionation corrections, employing software developed in-house for this purpose. Blank corrections for Pb (10±5 pg), together with isotope-dilution calculations, were performed using the algorithm published in ref. *37*. U blanks were negligible. Further details on the U-Pb data treatment can be found in ref. *20-22*.

The majority of previous U-Pb dating studies of speleothems have used isochron approaches to calculate sample ages (e.g. *20-22, 37, 38*). Although such an approach is undoubtedly the most robust, it is difficult to employ when attempting high-resolution chronologies because it uses large amounts of sample and is very time intensive. Following successful determination of 20 isochrons on the studied speleothems, we instead adopted a single-aliquot approach to increase the resolution of the age model. This methodology has been discussed elsewhere (*20-22*) but, in brief, where common Pb compositions either in one speleothem or in the same cave site are well constrained, and when the speleothems are relatively radiogenic, the mean estimate of common Pb based on previously determined isochron data, and its uncertainty, can be used in the calculation of model ages based upon single-aliquot analyses (*20*). The U-Pb dating of CC8 was the first documented example of using this method (*20*). This approach has since been updated, taking into account an improved estimate of the common-Pb composition for these stalagmites by addition to the previous dataset of one new isochron for CC8 and 13 isochrons for stalagmites CC119 and CC122 (fig. S1). Data from these new isochrons refined the previously published common Pb estimate from 0.818 +0.006/-0.011 to 0.81341 +/-0.00483 (fig. S2), although we stress that the new mean value is within the previously estimated 95% uncertainty of *ref. 20*.

In general, isochrons for stalagmites CC122 and CC119 have a better fit (i.e. a lower MSWD) than the previously published CC8 isochrons (*20*) (fig. S1). This is the result of a larger spread in isotopic ratios for these samples as well as their higher Pb content, which enabled improved precision in isotopic measurements for individual aliquots. However, as demonstrated in ref. *22*, application of a single-aliquot approach to relatively unradiogenic samples results in less accurate and precise ages. For this reason, we employed a filter and rejected from the age-depth modeling all samples with $^{238}U/^{206}Pb$ ratios lower than 2500. The rejected samples are marked with superscript R in Table S1. However, we stress that their inclusion in the age-depth modeling would affect neither the mean model age nor its uncertainty due to their large age uncertainties, which are, in almost all cases, >25 kyr. Three additional samples (fig. S2) were identified as outliers and also excluded from the age-depth modeling.

Since speleothems are often deposited out of secular isotopic equilibrium with respect to initial $^{234}U/^{238}U$ activity (*39*), thus necessitating a disequilibrium correction, we chemically prepared and measured $^{234}U/^{238}U$ isotope ratios on an aliquot of each sample separately (*40*). The analyses were performed on the Nu Instruments Plasma MC-ICPMS at The University of Melbourne. Uranium isotopic reference materials NBL-112A and HU-1 were used to correct for external

$^{234}U/^{238}U$ variability. Disequilibrium-corrected U-Pb ages and their uncertainties were calculated using an in-house macro (*20*). All isotope ratios and the final ages corrected for initial disequilibrium effects are provided in Table S1.

3. Compilation of the Corchia Cave speleothem stack

We developed a composite isotope series following the procedure used to produce a Corchia Cave $\delta^{18}O$ stack for the Last Interglacial (*23*). We first synchronised the CD3, CC30, CC119 and CC122 records to the depth scale of CC8 (fig. S4a), which has the longest record of the four dated stalagmites. The cross-tuning was based on pattern-matching both $\delta^{18}O$ and $\delta^{13}C$ profiles. The offsets between the stalagmite and CD3 $\delta^{13}C$ profiles are not surprising: percolation waters feeding each stalagmite pass through a unique fracture system causing different hydrogeochemical evolution pathways, whereas CD3 records the response to the 'population' of drips entering a large pool.

Stalagmite CC8 contains two hiatuses, at 337 mm and 355.5 mm depth. These are convincingly spanned by CC30 (the younger hiatus) and CD3 (both hiatuses); there is good agreement among the speleothems in the $\delta^{18}O$ and $\delta^{13}C$ profiles either side of each hiatus. We then developed a 'synthetic' stack depth scale that takes into account the need to add depth segments through both hiatuses of CC8, as well as to accommodate the growth of CC122 beyond the base of CC8 (i.e. below ~824 mm). For the older CC8 hiatus, the spacing between the five isotope data points of CD3 that span this hiatus was increased to account for the ~13x faster growth rate of CC8 compared to CD3 over the whole period of overlap for the two speleothems. For the younger hiatus, the spacing of the 13 isotope data points of CC30 that span this hiatus was decreased to account for the ~3x faster growth rate of CC30 compared to CC8 over the whole period of overlap for these two speleothems. Since the CC8 record between the two hiatuses (corresponding to 337.0 to 377.1 mm from the top of composite depth scale) is of very low resolution, we inserted the higher resolution CC30 and CD3 stable isotope data. Finally, for the base of CC122, which covers the oldest part of the stacked record, the spacing of each sampling point was reduced to 0.5 mm, compared to the original 1 mm. This accounts for the ~2x faster growth rate of CC122 compared to CC8 over their entire period of overlap. The final stacked series are shown as the grey curves in fig. S4a.

Further support for the match between the stalagmites comes from their individual age-depth models: the age-depth model for each of CC30, CC119 and CC122 overlaps within its respective uncertainties with that of CC8 (fig. S3a).

To place the composite stable isotope series onto an age scale, an age-depth model (ADM) was developed through the entire population of U-Pb ages on the abovementioned stack depth scale using a Monte-Carlo-based Finite Positive Growth Rate Model (*41-43*) (fig. S3b). Input parameters in this ADM approach are sample age and depth for each age determination together with their uncertainties. For each iteration of the model, age and depth for each sample are randomised according to their uncertainties, then sorted by their randomised depths and a least-squares procedure used to find the sequence of connecting positive growth rate age-depth line segments which best fit the uncertainty-weighted age-depth data. For each iteration, the algorithm also attempts to minimise the sum of the squares of relative growth rate change between adjoining age-depth line segments, subject to a user-controlled weighting factor that balances the importance of this against maximizing model fit to the measured ages (*41*). Where this weighting is too far in favour of a strict fit to age data, the resulting ADM can exhibit implausibly high swings of growth rate between adjacent samples; if too far in favour of minimizing growth rate change, the resulting ADM can appear insufficiently fitted to the age data. An acceptable range of growth-rate-minimization weighting factors was determined visually for the age-depth model after which that factor was randomized within this range for each of the 10,000 iterations of the Monte-Carlo ADM determination. The 3rd-, 50th- and 97th-percentile interpolated ages were determined at 500 evenly spaced steps along the stack depth scale and interpolated to give age and its uncertainty at any depth (*41, 43*) (fig. S3c). A review of diverse speleothem age-depth modelling procedures, including a version of the algorithm used here, found minor differences for sparsely-spaced age determinations but concluded that differences between model approaches were not significant for densely spaced age data (relative to uncertainty) (*42*), as is the case for this study. Similarly, the use of the growth-rate-minimisation weighting factor, which can have significant effect on the form of ADMs for sparse age data, has little influence in this case. This is confirmed by good correlation between our age-depth modelling output and another ADM approach (Bacon) described later in the text.

Where the age uncertainties of many individual age determinations overlap in time, ADM uncertainty (determined using any ADM technique) can be considerably smaller than that of individual ages (similarly to the calculation of a weighted mean of repeat age determinations of a single age horizon where uncertainly of the mean age is reduced by approximately the square root of the number of repeat measurements). This reduction of uncertainty is only valid where individual ages have independent, uncorrelated uncertainties, i.e. where there is no common source of uncertainty. Following ref. *20*, we have assumed that the initial ^{207}Pb/^{206}Pb ratio uncertainty determined on the basis of isochron determinations (fig. S2) is composed of equal components of correlated (i.e. common to all samples, arising from imprecision in the determination of mean initial value) and uncorrelated (i.e. due to natural variability between age measured samples). Three ADMs were calculated using ages calculated with the median, upper and lower bounds of the correlated initial ^{207}Pb/^{206}Pb and the difference between their median ADM curves used to determine the correlated component of age uncertainty, which was then added to the uncertainty envelope derived using uncorrelated initial ^{207}Pb/^{206}Pb variability about its mean value. This approach is described in greater detail in ref. *20* with the difference that, here, isochron ages are used alongside single-aliquot ages in the ADM where available instead of choosing the most radiogenic single-aliquot age from each individual isochron set. This modification was introduced to acknowledge that the results based on the isochron method are more robust as they do not rely on globally estimated common Pb composition and are free of significant correlated uncertainty. Corchia Cave speleothems are amongst the least-contaminated by detrital thorium ever reported, with ^{230}Th/^{232}Th activity ratios of over 100,000 measured in each of the three stalagmites studied here, substantially in excess of the suggested minimum value of 1000 at which U-Th age corrections can typically be considered insignificant (*44*).

4. Foraminifer stable isotope and alkenone SST analyses

Data from two ocean-sediment cores were used in this study. From Integrated Ocean Drilling Program (IODP) Site U1385 (36.8° N, 7.7° W) (*30*), we assembled new, high-resolution planktic and benthic foraminifer $\delta^{18}O$ series to complement the published $\%C_{37:4}$ data; the published SST series from this Site (*31*) are insufficiently resolved for comparing with the high-resolution foraminifer $\delta^{18}O$ data, so we assembled a new $U^{k'}_{37}$ biomarker-based SST and planktic $\delta^{18}O$ series from IODP Site U1387 (*45*) (36.5°N, 7.43°W). The surface-water composition of both sites is similar on account of their close proximity (*46*), enabling the two ocean-core records to be synchronized (fig. S5).

The new planktic and benthic $\delta^{18}O$ series from Site U1385 presented here expand the previously published low-resolution data (*30*). The core was sampled along the spliced composite section at a constant sample spacing of 2 cm. Stable isotopes were measured on the planktic foraminifer *Globigerina bulloides* selected from the 250- to 355-μm size fraction and the benthic foraminifer *Cibicidoides wuellerstorfi* from the >212-μm fraction. Foraminifer tests were cleaned prior to analysis (*30*) and isotopic analyses performed using a VG SIRA mass spectrometer with a Multicarb system for samples with a mass exceeding 80 μg. Analytical precision (1σ) is estimated to be ±0.08‰ for both $\delta^{18}O$ and $\delta^{13}C$. For smaller samples (<80 μg), measurements were performed on a Thermo Finnigan MAT253 mass spectrometer fitted with a Kiel device. Analytical precision (1σ) is estimated to be ±0.08‰ for $\delta^{18}O$ and ±0.06‰ for $\delta^{13}C$, respectively. Results are reported relative to V-PDB. All isotope measurements were made in the Godwin Laboratory, University of Cambridge.

For Site U1387, the alkenone-derived SST and planktic $\delta^{18}O$ series were reconstructed from cores U1387A-22X to U1387A-25X and U1387B-21X to U1387B-24X (*47*). Sample spacing was adjusted to avoid coring disturbances (biscuiting) but yields an average resolution of 12-13 cm (approximately 390 yr) for the planktic $\delta^{18}O$ record and 24-26 cm (780 yr) for the SST record. The resolution of both records was increased to an average of 6 cm during the MIS 22-21 transition (TX). Stable-isotope analyses were conducted on the foraminifer *Globigerina bulloides* on between 8 and 15 specimens collected from the >250-μm fraction (*46*). The samples were measured on either a Finnigan MAT 251 or 252 mass spectrometer coupled to an automated Kiel I carbonate preparation system, at MARUM (University Bremen, Germany). The long-term precision (1σ) is ±0.05‰ for $\delta^{13}C$ and ±0.07‰ for $\delta^{18}O$ based on repeated analyses of internal (Solnhofen limestone) and external (NBS-19) carbonate standards.

For the U1387 SST reconstruction (*31, 45, 48*), the molecular lipids (including alkenones) were extracted from the freeze-dried, ground sediment samples by sonication using dichloromethane. After hydrolyzation with 6% potassium hydroxide in methanol to eliminate interferences from wax esters, the neutral lipids were then extracted with hexane, evaporated to dryness under a nitrogen gas stream then finally derivatised with bis(trimethylsilyl)trifluoro-acetamide. The lipids were analyzed on the DivGM's Varian Gas chromatograph Model 3800 equipped with a septum programmable injector and a flame ionization detector (*31, 49*). Annual mean SST was calculated from the alkenone unsaturation index $U^{k'}_{37}$ (*50*) using the equation from ref. *51*.

5. Synchronization of the U1385 and U1387 ocean records to the Corchia Cave speleothem time scale

The data from Site U1385 were anchored to the Corchia Cave chronology by synchronizing the planktic $\delta^{18}O$ to the speleothem $\delta^{18}O$. The rationale for this approach is as follows. Previous studies on Corchia speleothems (*19, 26, 52*) argued that millennial-to-orbital-scale changes in the speleothem $\delta^{18}O$ are responsive to variations in SST in the North Atlantic and western Mediterranean Sea. Under this scenario, a warmer SST results in greater moisture advection from the North Atlantic to the cave site, increasing the quantity of rainfall and lowering the rainfall (and speleothem) $\delta^{18}O$ via the 'amount effect' (*53*). The converse occurs during periods of SST cooling. The dominance of the amount effect is reinforced by the local topography at the cave site, where the mountains rise to almost 2000 m above the nearby coastal plain and constitute an imposing orographic barrier. However, it has been argued that during a termination Corchia speleothem $\delta^{18}O$ can be affected by meltwater released from decaying continental ice-sheets around the North Atlantic margin (*27*). Regional planktic $\delta^{18}O$ is a function of the temperature of (bio)mineralization and the $\delta^{18}O$ composition of the source waters, and except during periods of large-scale meltwater flux, source-water changes are minimal, causing the planktic $\delta^{18}O$ to closely track SST (*28*). However, meltwater pulses during terminations cause a lowering of surface ocean $\delta^{18}O$ that more than counters the effect of reduced ocean temperature on planktic $\delta^{18}O$, causing a decoupling between the planktic $\delta^{18}O$ and SST (*27, 29*). This is seen vividly during the well-studied TII interval, where SST, the tetraunsaturated alkenone $C_{37:4}$, and the planktic $\delta^{18}O$ show the combined and unequivocal effects of cooling and freshening of the surface ocean as ice-sheet meltwaters penetrated southwards to the Iberian margin and entered the western Mediterranean Sea (*27, 29*). As the predominant sources of water vapour reaching Corchia Cave are of North Atlantic and western Mediterranean origin (*19*), the $\delta^{18}O$ of air masses reaching Corchia would be directly influenced by large-scale, meltwater-driven changes in surface-ocean $\delta^{18}O$, such as those that occur during a termination. This is supported in principle by a recent study using an isotope-enabled Earth-system model, which shows a depletion in precipitation over Greenland and Brazil during meltwater events (*54*). Thus, the speleothem and planktic $\delta^{18}O$ share a common set of drivers, making the planktic $\delta^{18}O$ a more robust tuning target than SST, as previously argued (*26*). This is evident in the strong structural similarity between the speleothem and planktic $\delta^{18}O$ series (Fig. 1 and fig. S4b), whereas the similarity between the speleothem $\delta^{18}O$ and SST is somewhat lower, particularly at the sub-orbital scale. Nevertheless, assigning the SST series, rather than the planktic $\delta^{18}O$ series, as the tuning target would make no age difference in the case of TXII and would lower the age estimate by not more than 2 kyr in the case of TX.

To complete the synchronization procedure, the Site U1387 data were tuned to the depth scale of Site U1385 using their respective planktic $\delta^{18}O$ series (fig. S5). The Corchia chronology for Site U1385 was then interpolated to the Site U1387 record, enabling the SST series from the latter to be placed onto the same time scale as the speleothem stack, and the U1385 planktic and benthic $\delta^{18}O$ and $C_{37:4}$ alkenone series. The two synchronizations were implemented in *AnalySeries* (*55*) by selecting as chronostratigraphic markers a series of control points that define oscillations assumed to be common to both records (fig. S4b and S5).

The resulting age model for Site U1385 (herein referred to as 'CC-Raw') yielded sedimentation rates ranging between 0.02 and 0.85 m kyr^{-1}, which exceeds those determined from an earlier study that considered four alternative age models (Table S2) (*30*). Whilst an increase in the amplitude of sedimentation rates can be expected due to the higher density of control points used in our tuning, the final age model should still yield a plausible range of sedimentation rates. The largest source of error in the cave-ocean correlation that can lead to extreme sedimentation rates stems from the fact that only the ocean series is 'moved' during the tuning process, whereas the speleothem series remains fixed in time despite radiometric age uncertainties that, for the majority of the record, exceed 3 kyr (fig. S3c). To account for this, the U-Pb model ages and age uncertainties for each control point were combined with a Monte Carlo approach to derive two alternative age-depth models for Site U1385, with sedimentation rate employed as a constraint. The first was implemented using the software *Bacon* (*56*) in the statistical package R and is based on 91 x 0.2 m sequential sections of Site U1385, with the following parameter settings: a mean accumulation rate of 0.1 m kyr^{-1}; an accumulation shape of 1.5; a memory strength of 4; and a memory mean of 0.7. A total of 50,000 Markov Chain Monte Carlo iterations were performed, producing the model shown in fig. S6 (herein called 'CC-Bacon'). The second simulation was conducted using the Finite Positive Growth Rate Model employed to generate the original Corchia speleothem age model shown in Fig. S3b (herein called 'CC-FGR'). Here, the model was adjusted to accommodate a mean sedimentation rate of 0.10 m kyr^{-1} and allowing the sedimentation rate to vary by a factor of approximately three around this mean value, consistent with the earlier models (*30*). The output is shown in fig. S6, along with the derived sedimentation rate ranges, which are compared against the planktic $\delta^{18}O$ on the CC-Raw time scale. The sedimentation rate statistics and termination ages for each model are summarised in Table S2.

The CC-Bacon and CC-FGR simulations produced U1385 age model ages that fall within the age-model envelope of the CC-Raw model output. The derived TX and TXII age estimates deviate by no more than 13% of the total age-error envelope of the CC-Raw model (i.e. they are well within 1σ uncertainty). We therefore use the CC-Raw age model output to assign age estimates and uncertainties for TX and TXII (Fig. 2; Table S2).

The CC-Bacon and CC-FGR sedimentation rates generally follow the Site U1385 planktic δ^{18}O, but whilst low sedimentation rates are broadly associated with higher planktic δ^{18}O values (i.e. cooler climate) and *vice versa* over the older half of the record, the pattern clearly reverses at ~900-890 ka for the remainder of the record. The glacial maximum of MIS 22 and the early part of TX, in particular, show large sedimentation rates. Such spikes in sedimentation rate have also been observed in the directly dated sequence through TI in nearby core MD99-2334 (*57*). Broadly the opposite occurs during TXII. The reason for this reversal is unclear but could signal a change in the pattern of deep-ocean currents associated with the MPT.

6. Identifying the start of Terminations XII and X

Criteria for the timing of terminations vary (*5, 9, 13, 26*). In this study we focus firstly on the timing of the *onset* of terminations. For TXII and TX we identified this onset as the point where SSTs, planktic δ^{18}O and $C_{37:4}$ values show evidence of deglacial meltwaters reaching the Iberian margin, which together provide firm evidence of the collapse of Northern Hemisphere ice sheets (terminal stadial events). For both TXII and TX, the Site U1385 benthic δ^{18}O values also start their near-monotonic trajectory towards interglacial values at these positions. Such multi-proxy coherence provides firm constraints on the core-depth positions for both TXII and TX. The Site U1385 depth positions used for the start of TXII and TX are 100.56 m and 110.08 m (i.e. crmcd as defined in ref. *30*) respectively. Ages interpolated from each age model are shown in Table S2. They clearly show that the model estimates are statistically indistinguishable (reduced chi-square statistic (MSWD) 0.47, probability of fit 0.62; statistically significant at $p < 0.05$). To calculate the 95% age errors presented in Table S2, we combined in quadrature the age modelling uncertainty for each model simulation (using the larger value of the plus or minus errors) with a conservative estimate of the synchronization uncertainty (±2 kyr).

For the period covered by the Corchia speleothem record, we only focus on the full deglaciations of TX and TXII, which are well expressed in the two ocean records. We do not consider the ‘skipped deglaciation’ of TXI due to uncertainties in aligning the marine record to the Corchia δ^{18}O over this time period. This is evident in the lower number of tuning points between 920 and 900 ka (fig. S4b). Nevertheless, based on the Corchia-tuned ocean record, the skipped termination occurs at ~914 ka (Fig. 1), placing it ~one obliquity cycle from both TXII and TX. The reason for the mismatch between the speleothem and ocean records is not entirely clear; even the two planktic δ^{18}O series show different patterns during this transition, making it very challenging for synchronisation.

7. A register of termination timings and durations

The following two sections provide supporting information for the data presented in Figures 3 and 4, which compares the phasing of astronomical and insolation metrics to the timing of radiometrically constrained terminations from the present study (TXII and TX) as well as those from previous studies (*15, 17*). As discussed in the main text, terminal stadial events

– intervals of extensive ice-rafting, freshwater incursion and cooling in the North Atlantic Ocean that occur during a termination – can be used to determine when TXII and TX commenced. The timing of Terminations I to VII (which includes two deglaciations (TIIIa and TVIIa) widely acknowledged as being large enough to be assigned 'termination status' – *ref. 58*), has been determined using speleothems from China (*15, 17*). The $\delta^{18}O$ of these speleothems is sensitive to changes in the status of the Asian Summer Monsoon. Terminal Heinrich events trigger large-scale changes in ocean and atmospheric circulation, including a southward migration of the Intertropical Convergence Zone (ITCZ), which is thought to be responsible for the increase in $\delta^{18}O$ in Chinese speleothems during these events (*59*). These cause a weakening of the Asian Summer Monsoon (ASM) - so-called 'Weak Monsoon Intervals' (WMIs) (*17*) – although several mechanisms have been proposed (*60*). Precise U-Th chronologies at the initiation of WMIs provide accurate estimates of the onset of the terminations in which they are contained through alignment with the corresponding terminal stadial event recorded in North Atlantic ocean cores. In the case of TIIIa to TIV, marine proxies from drilling site ODP980 (*61*) are used for the alignment, whilst data from site U1314 (*62*) are used for TV to TVII (*15, 17*). Chronologically well-constrained ocean and sea-level records through TI (*63*) and TII (*64*) support the veracity of Chinese speleothem $\delta^{18}O$ to respond rapidly to the initiation of terminal stadial events, irrespective of the exact atmospheric teleconnections involved. Together with the results of the present study, the timing of the onset of 11 of the last 13 terminations can now be constrained radiometrically (Table S4). Figure S7 shows the context of each of these termination onsets against the relevant North Atlantic ocean records (*61, 62*) as well as the LR04 benthic $\delta^{18}O$ stack (*5*).

Determining the duration of each termination ideally requires a radiometric age estimate of when ice volume reached its minimum in the ensuing interglacial. For TI and TII, this is relatively straightforward due to the large number of U-Th ages on corals that constrain the age of the MIS 5e and MIS 1 sea-level high stands. We assign an age of 7 ka for the end of TI based on the data compilation of *ref. 63*, and an age of 129 ka for the end of TII based on evidence presented in *ref. 64* (Table S3). For TIIIa to TVII, the issue is more challenging: the link between the status of the ASM and the attainment of minimum ice volume during the following interglacial is unclear, precluding the direct assignment of a speleothem age to the approximate position of the termination end in the ODP980 and U1314 ocean records or the LR04 benthic $\delta^{18}O$. Instead, we identified the end of deglaciation as the point in the LR04 benthic $\delta^{18}O$ stack where the first derivative of a two-point smoothing of the $\delta^{18}O$ crosses the 'zero line' within the interglacial (i.e. where the direction of benthic $\delta^{18}O$ change in successive data points through the deglaciation switches from positive to negative) and where the termination is obviously complete based on ~minimum benthic $\delta^{18}O$ values (lower panels, fig. S7; Table S3). The age assigned to this point was adjusted by an amount equivalent to the difference between the LR04 and the speleothem-derived ODP980 or U1314 benthic $\delta^{18}O$ ages for the *start* of the termination; determining the position of this point on the LR04 stack from ODP980 and U1314 was relatively straightforward (fig. S7). Since the original age model of the LR04 stack is tied to assumptions based in orbital tuning for much of the time period we cover (*5*), we also estimated the timing of the completion of TIIIa to TVII using an alternative version of LR04 that is anchored to a depth-derived chronology (i.e. free of orbital-forcing assumptions) (*13, 14*). These estimates are provided in the lower panel of Table S3.

Since we have radiometric age control on the U1385 benthic δ^{18}O through TXII and TX, we assigned an age to their completion using similar principles to the above: we first applied a five-point smoothing (due to its higher resolution) to the U1385 benthic δ^{18}O then identified the point through the termination where the first derivative (fig. S7) switches to negative. Synchronization of the speleothem and ocean records at the end of TX was somewhat more challenging because there is a short interval in the speleothem stack that is represented only by the low-resolution record from CD3, a slow-growing subaqueous speleothem (fig. S4a). This affects the positioning of the end of TX. However, our derived age estimate (864 ka), which indicates a termination of intermediate length (~11 kyr), is consistent with the LR04 estimate of the duration of this termination (~12 kyr). Based on the termination commencement and completion ages graphically shown in fig. S7, the midpoint and duration for each termination can be derived (Table S3).

We should note that we considered assigning the end of each termination based on the LR04 threshold δ^{18}O values used by *ref. 9* in developing their register of interglacials. However, it is clear that deglaciation for most G-IG cycles continues well beyond the point where these thresholds are crossed and relying on these markers would significantly underestimate the termination duration.

8. Orbital and insolation metrics for each termination

We extracted orbital and insolation metrics at the onset, midpoint and completion ages for each termination (Table S4) to determine if phasing of climatic precession (herein precession) and obliquity for TXII and TX is any different to the earlier terminations, and what factors (if any) control the duration of terminations. Polar plots (Fig. 3a-c, main text) of the phasing of precession and obliquity at each termination onset, midpoint and ending were compiled by converting the astronomical data from *ref. 1* into degrees. Due to the unequal amplitude of these cycles, each half-precession and half-obliquity cycle was treated separately. Maximum obliquity and maximum precession (used here to represent times when perihelion aligns with the Northern Hemisphere summer solstice) of each cycle were both referenced to 0°, and the preceding minimum obliquity and precession were assigned a phase of 180°; intermediate values of both metrics were linearly interpolated. Due to their previous association as indices controlling terminations and the attainment of interglacial conditions, the caloric summer half-year insolation values at 65°N (*9*) and integrated summer energy (>275 W/m^2) at 65°N (*16*) were also extracted for the start, midpoint and end of each termination. Table S4 contains the metrics used to compile Figure 3.

In Figure 4b, we compare termination midpoint ages and their uncertainties (see next paragraph) to the insolation forcing time series of *ref. 13*, which combines both precession and obliquity variability in equal amounts. Briefly, the forcing at time t ($\mathcal{F}_t$) takes the form:

$$\mathcal{F}_t = \alpha^{0.5} e_t \sin(\omega_t - \phi) + (1 - \alpha)^{0.5} \varepsilon^t$$

where e is eccentricity, ω is the angle between the vernal equinox and perihelion and ε is tilt (each normalised to zero mean and unit variance), ϕ is zero degrees and α is 0.5 *(13, 67)*.

To construct Figure 4c, we proceeded as follows. We first estimated conservative age uncertainties for each termination based on radiometric ages (*15, 17*) or model ages (this study) for each termination onset. These uncertainties (as ± kyr, 95% confidence limits) were assumed to apply for midpoints and completions, and are as follows: T1: 0.2 kyr; TII: 0.5 kyr; TIIa and TIII: 1 kyr; TIV: 2 kyr; TV: 2.5 kyr; TVI: 4 kyr; TVIIa: 5 kyr; TVII: 6 kyr; TX: 5 kyr; TXII: 5 kyr. Second, for each of the three orbital metrics (i.e. obliquity, climatic precession and the insolation metric of *ref. 13* that combines obliquity and precession), phase uncertainties were derived using the age uncertainties for each termination. Therefore, for each termination age and 95% uncertainty, a corresponding phase mean and uncertainty was extracted for each of the three metrics. Probability distributions were then calculated, and a phase mean and its uncertainty derived for each metric (fig. S8). For this last step, we used the 'weighted-average function' in *Isoplot* (*65*), which calculates a mean and uncertainty that is weighted according to the magnitude of the individual uncertainties. In short, the lower the uncertainty of an individual age, the more weighting that age has in the calculation of both the overall mean and its uncertainty, and *vice versa*. Two of the 11 observations for obliquity and one of the 11 observations for climatic precession were identified by *Isoplot* as outliers (highlighted as the red distributions in Figures S8b and d); no outliers were identified from the combined precession and obliquity distributions (fig. S8e). *Isoplot*'s weighted-average function automatically identifies these outliers, which the user has the option of rejecting. In classical geochronology applications such as radiometric age determination from multiple sample aliquots, each aliquot is assumed to be part of the same chronostratigraphic layer or event and, where justifiable, outliers are removed. Outliers can result from, for example, analytical issues, contamination or open-system behaviour, or where aliquots (e.g. single mineral grains) truly belong to a different geological event or population. Since such criteria do not apply to our study of termination ages, the outliers noted above were not rejected. The composite probability distributions shown in Figure 4c were thus determined from the data plotted in Figures S8a, c and e.

Supplementary Figures and Tables

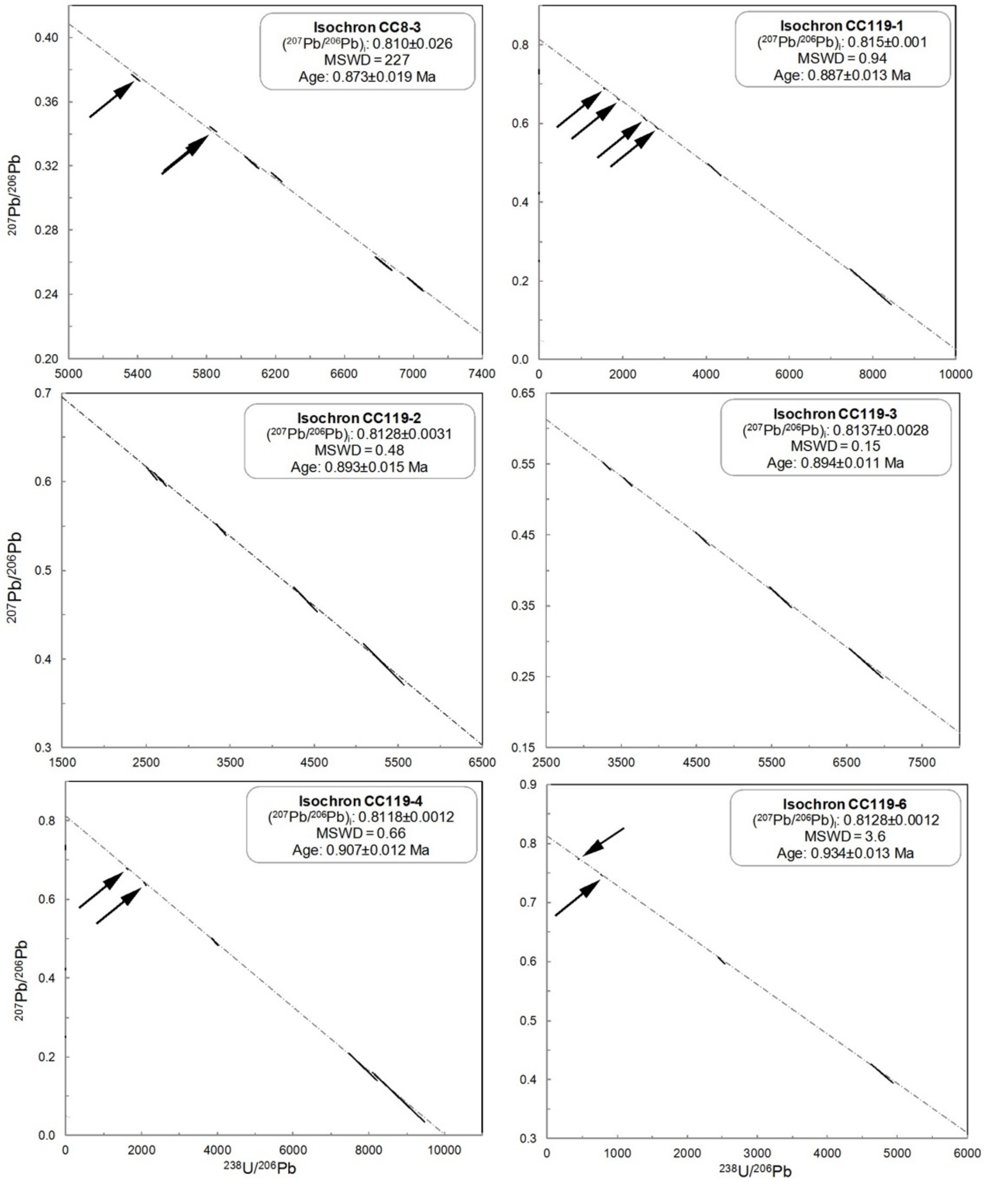

Fig. S1. Plots of CC8-3 and all CC119 isochrons. All ages are corrected for initial disequilibrium in the U-Pb decay chain.

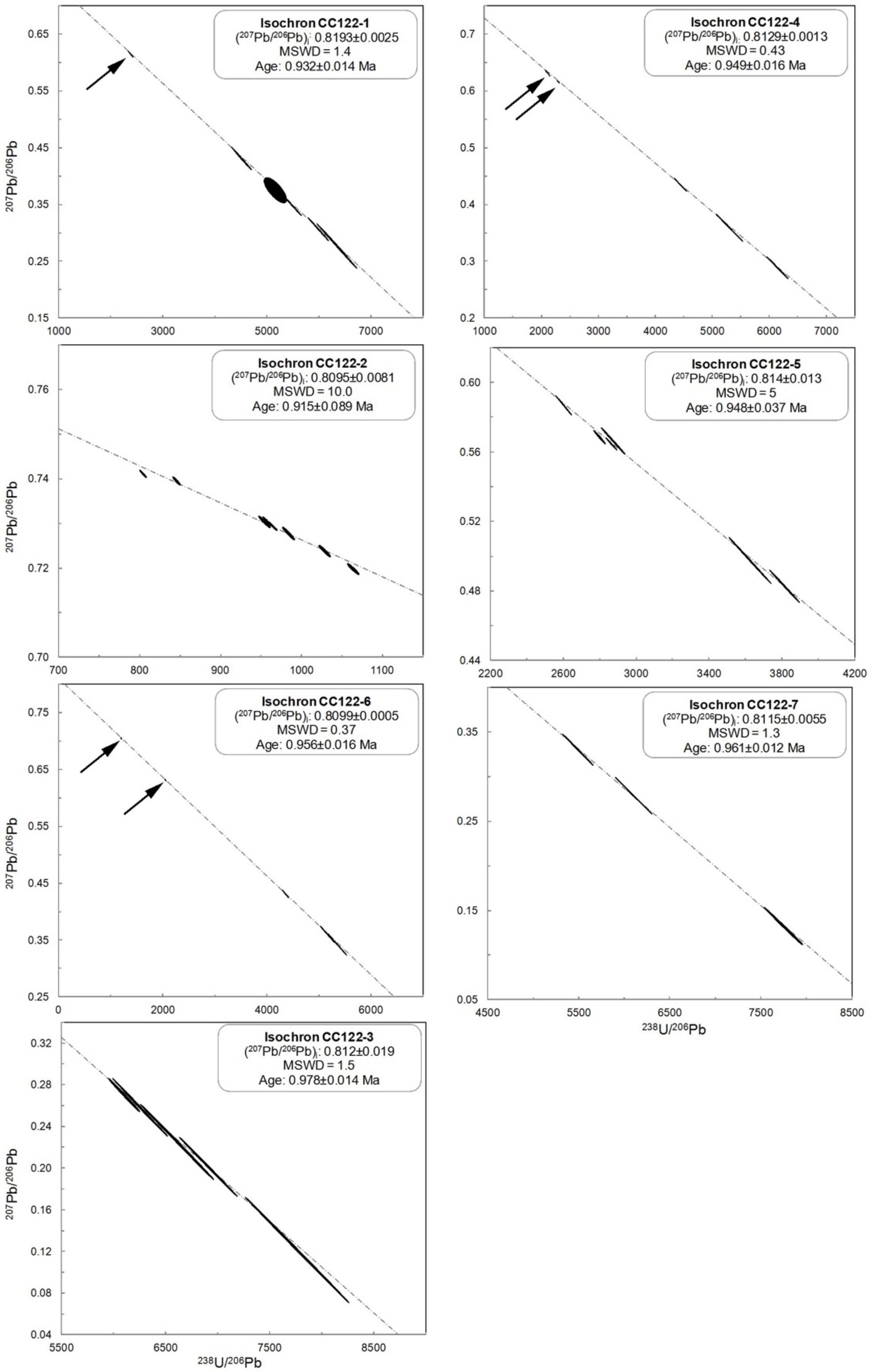

Fig. S1. (Cont.) Plots for CC122 isochrons. Based on these measurements an initial ^{207}Pb/^{206}Pb ratio was estimated and used to calculate single aliquot ages.

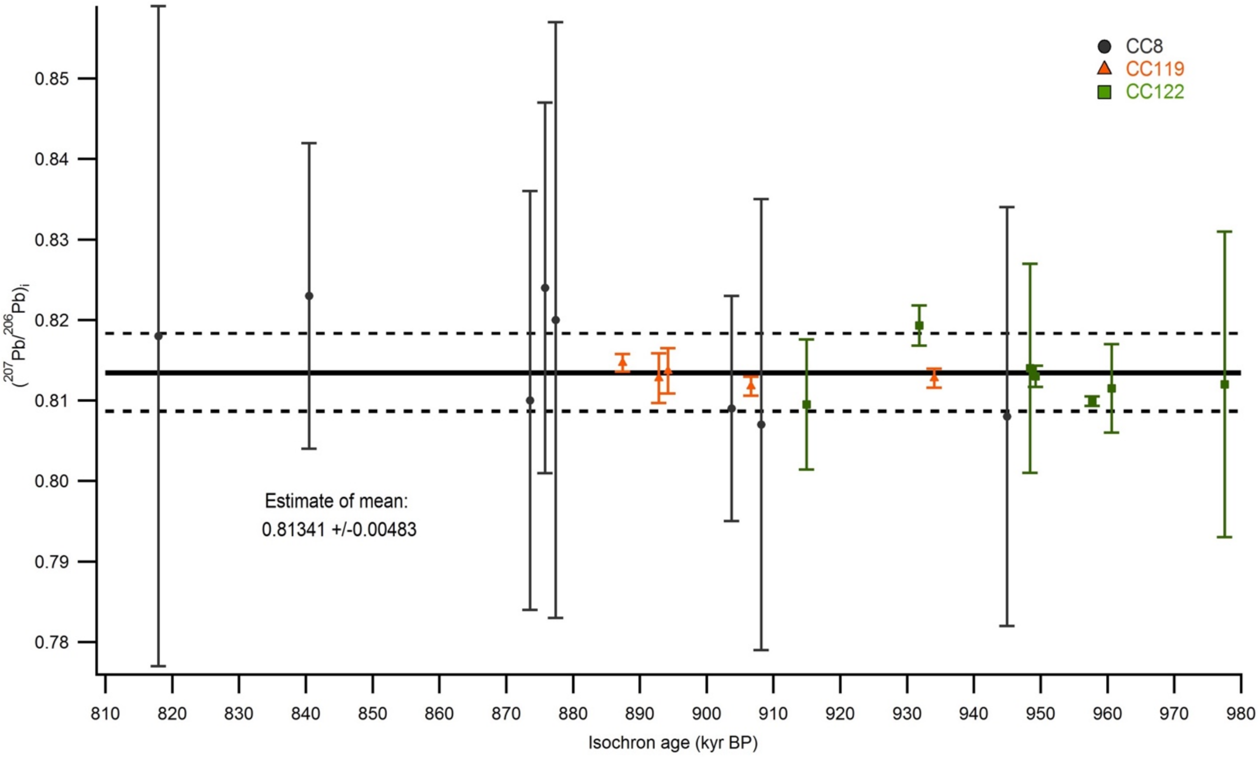

Fig. S2. Initial ^{207}Pb/^{206}Pb ratio for all 20 full isochrons determined in this study suggests a stable and consistent source of common Pb. The estimated mean is indicated with a thick horizontal black line while dashed lines present its 95% uncertainty.

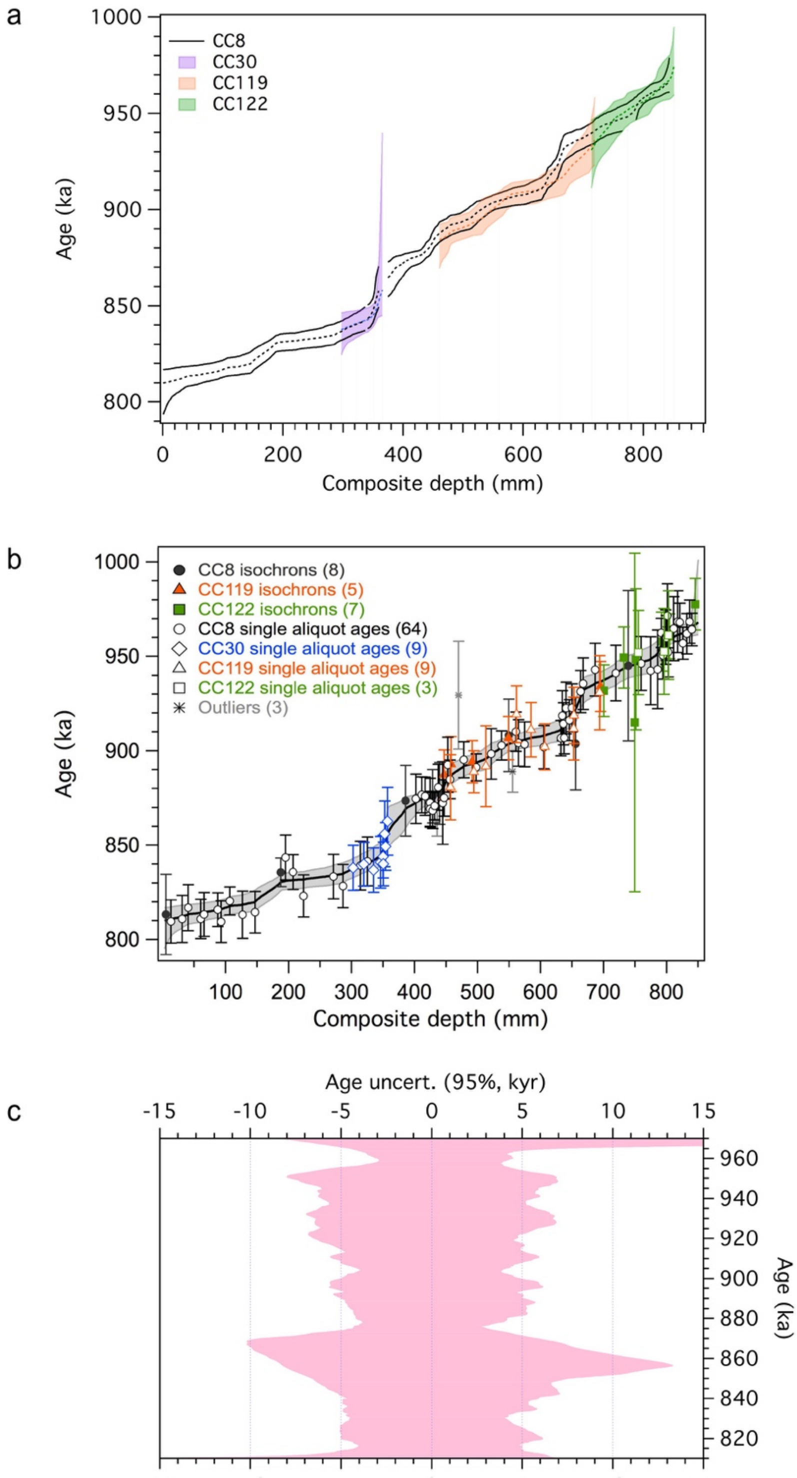

Fig. S3. (a) Individual age-depth model 95% uncertainty envelopes for Corchia speleothems CC8 (black lines), CC30 (purple shading), CC119 (orange shading) and CC122 (green shading). All speleothem data are plotted on the composite depth scale based on the cross-tuning of their respective $\delta^{18}O$ profiles (see fig. S4a and Materials and Methods for details). (b) The composite age-depth model produced from 20 isochron and 85 single-aliquot U-Pb ages. The three outliers shown are single-aliquot ages and are not included in the age-depth model. The median model age is represented by the solid black line. The grey shaded area is the 95% uncertainty envelope. (c) Age-for-age uncertainty based on the age model shown in (b).

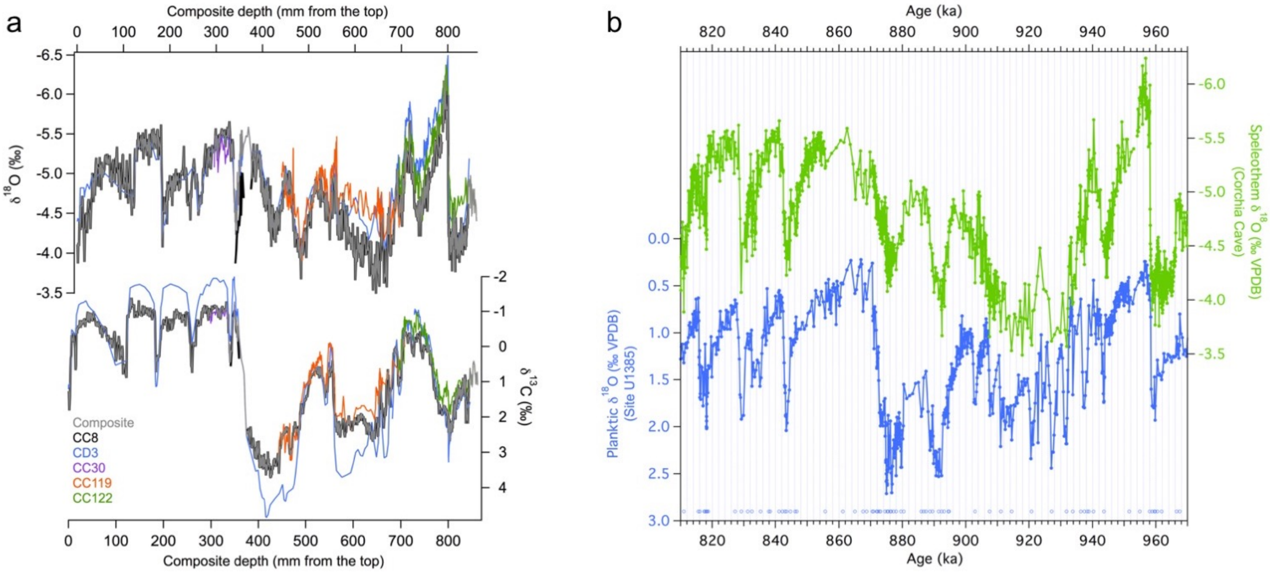

Fig. S4. (a) Stable isotopes series for all speleothems (CC8 in black; CC30 in purple; CC119 in orange; CC122 in green and CD3 in light blue) translated onto the composite depth scale using δ^{18}O and δ^{13}C as proxies for cross tuning. The composite profiles are shown in grey. (b) Results of the synchronisation of site U1385 marine to the Corchia Cave speleothem stack shown in (a). The synchronisation was achieved by correlating the speleothem δ^{18}O and planktic δ^{18}O records, and was implemented in *AnalySeries* (*55*). The plots are shown on the Corchia Cave U-Pb chronology. The open circles represent the tuning points used.

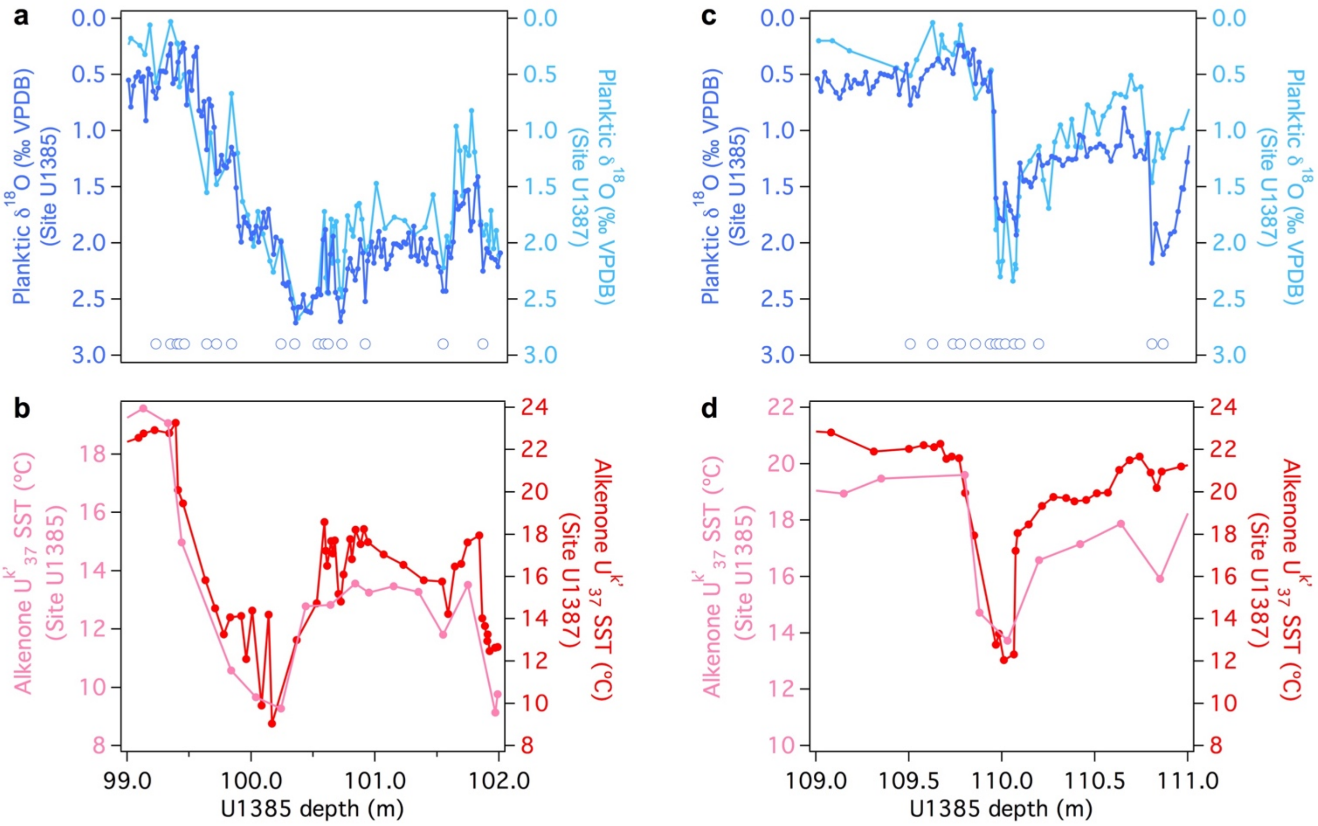

Fig. S5. Results of the synchronisation of ocean sites U1385 and U1387 for Termination X (a, b) and XII (c, d). The tuning was implemented in *AnalySeries* (*55*) using the two planktic δ^{18}O records. The corresponding alkenone $U^{k'}_{37}$ SST series from each core are also shown. Each plot is displayed on the depth scale of U1385. The open circles are the tuning points used.

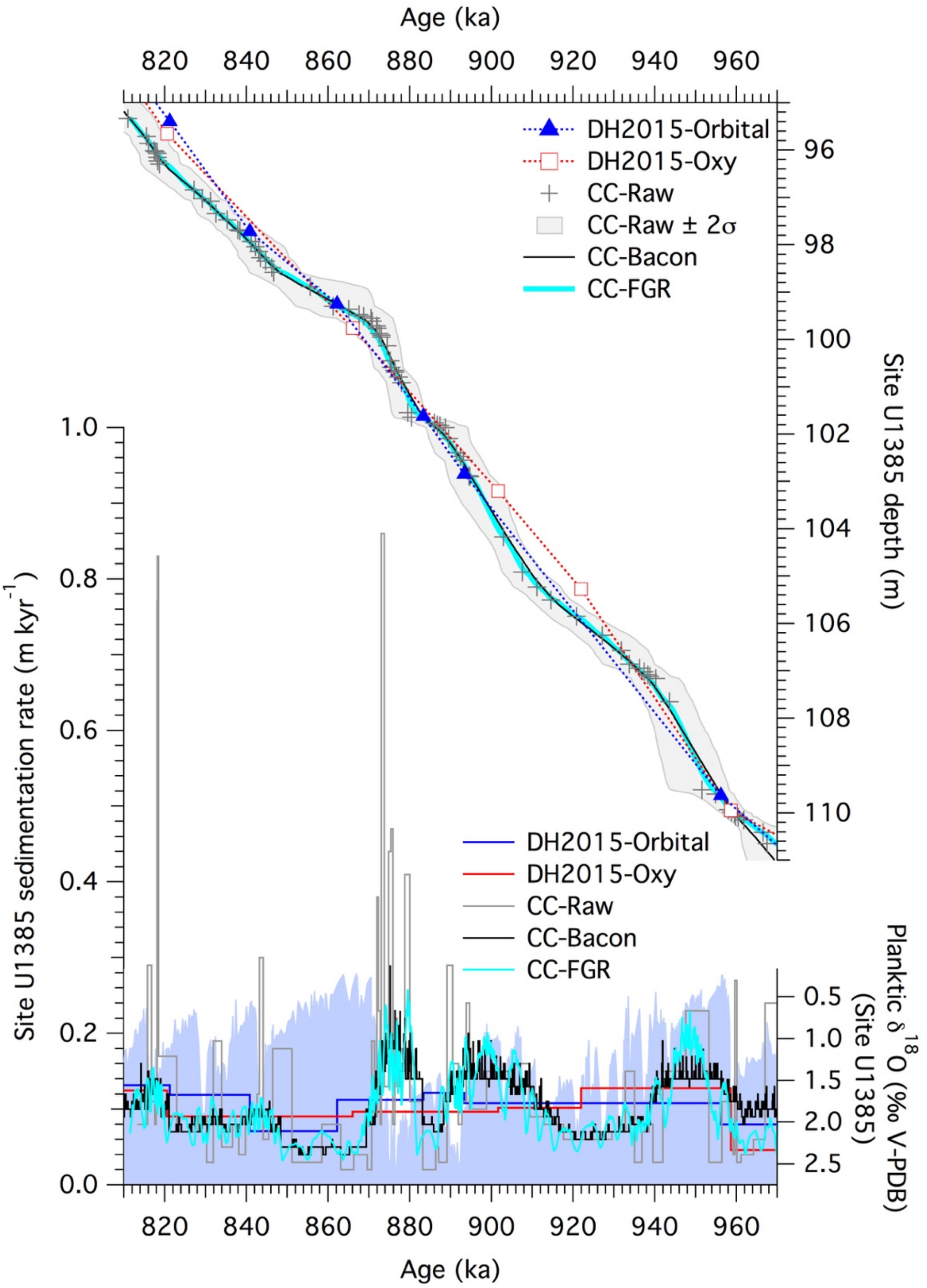

Fig. S6. Age models (upper panel) and sedimentation rates (lower panel) for Site U1385 using the published DH2015-oxy and DH2015-orbital models (*30*), and the CC-Raw, CC-Bacon and CC-FGR outputs derived from this study. The planktic δ^{18}O data are also shown (lower panel) on the CC-Raw age model for comparison with sedimentation rates. See Materials and Methods for an explanation of these models.

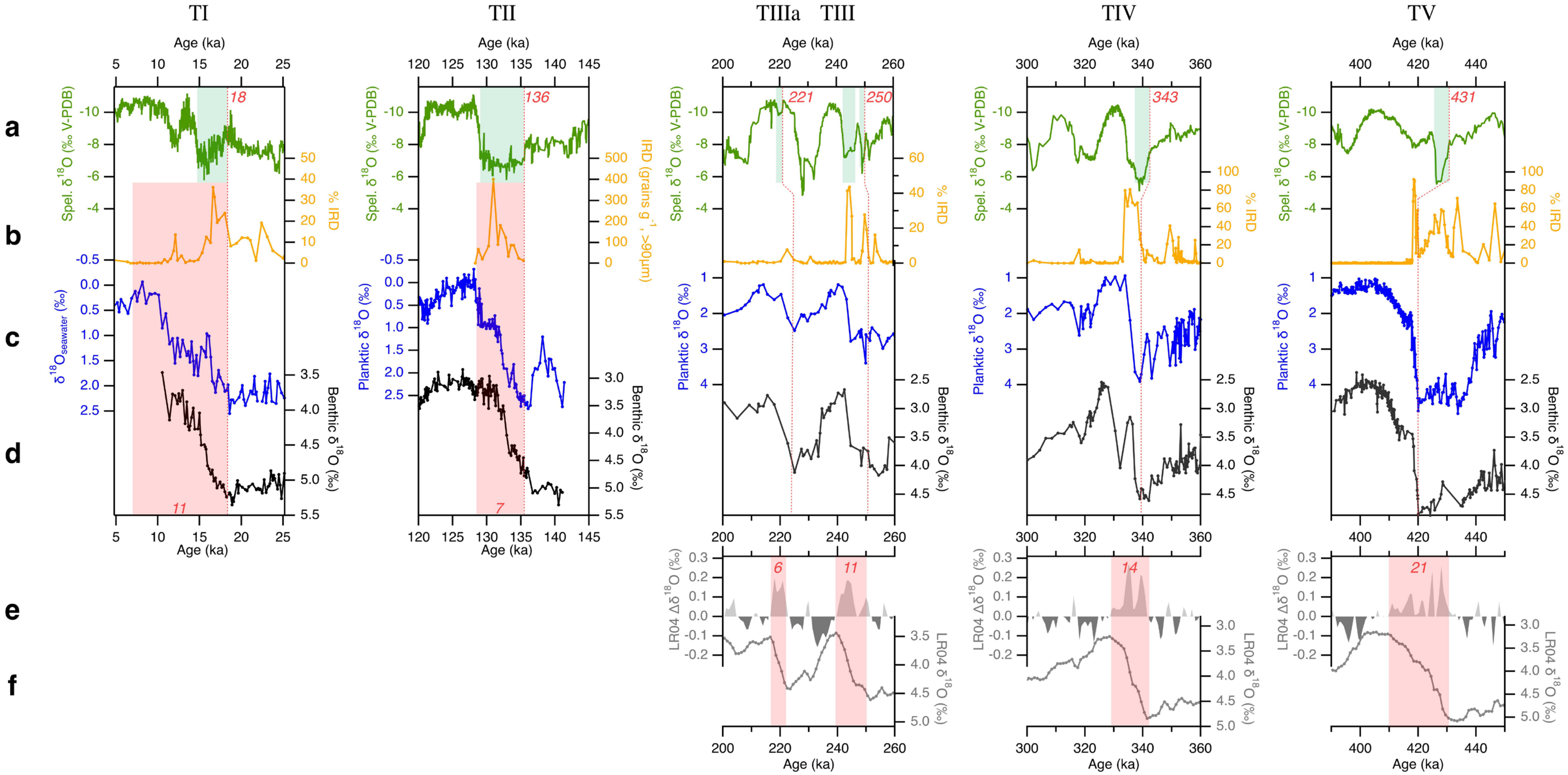
TI
TII
TIIIa
TIII
TIV
TV
a
b
c
d
e
f
Age (ka)
Spel. δ18O (‰ V-PDB)
% IRD
IRD (grains g-1, >90µm)
δ18Oseawater (‰)
Planktic δ18O (‰)
Benthic δ18O (‰)
LR04 Δδ18O (‰)
LR04 δ18O (‰)
18
11
136
7
221
250
6
11
343
14
431
21

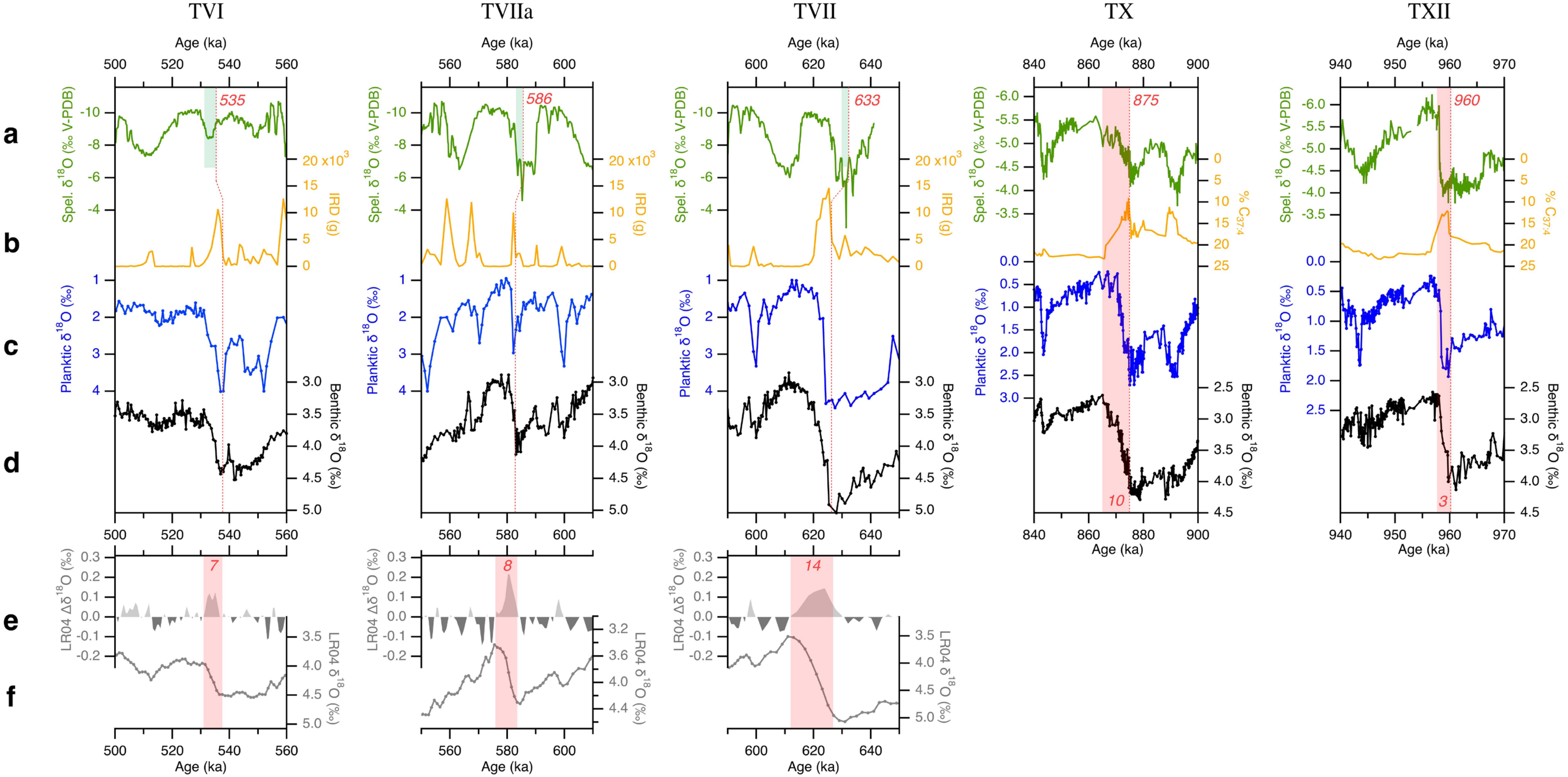
TVI
TVIIa
TVII
TX
TXII
Age (ka)
500
520
540
560
580
600
620
640
840
860
880
900
940
950
960
970
a
b
c
d
e
f
Spel. δ18O (‰ V-PDB)
-10
-8
-6
-4
-6.0
-5.5
-5.0
-4.5
-4.0
-3.5
IRD (g)
20 x10³
15
10
5
0
% C37:4
25
20
15
10
5
0
Planktic δ18O (‰)
1
2
3
4
0.0
0.5
1.0
1.5
2.0
2.5
3.0
Benthic δ18O (‰)
3.0
3.5
4.0
4.5
5.0
2.5
535
586
633
875
960
10
3
LR04 Δδ18O (‰)
0.3
0.2
0.1
0.0
-0.1
-0.2
LR04 δ18O (‰)
3.2
3.6
4.0
4.4
7
8
14

Fig. S7. Speleothem-based radiometric ages for the commencement and duration of TI – TVII and TX and TXII. **(a)** Speleothem records (green curves) from Hulu, Dongge and Sanbao Caves (China; TI to TVII) (*15, 17*) and Corchia Cave (Italy; this study: TX and TXII). **(b) - (d)** North Atlantic Ocean records from drilling sites MD99-2334K (TI: *ref. 57*), MD01-2444 (TII: *ref. 23*), ODP980 (TIIIa – TIV: *ref. 61*), U1314 (TV – TVII: *ref. 62*), and U1385 (TX and TXII: this study). The blue curves (b) are all planktic d^{18}O records except that for TI, which shows the temperature-corrected (using Mg/Ca) surface ocean-water δ^{18}O (*57*). The orange curves (c) show ice-rafted debris concentrations for all terminations except TX and TXII, for which the percent Uk' $C_{37:4}$ freshwater proxy is shown instead. The black curves (d) show benthic δ^{18}O through each termination. **(e) - (f)** For TIIIa to TVII, the LR04 benthic δ^{18}O stack (*5*) is also shown with a two-point smoothing applied (f) and its first derivative (e). Ages for the commencement of each termination (red italicised numbers shown in each of the speleothem plots) are from U-Th or U-Pb dates. For TI – TVII, these estimates are based on the start of 'Weak Monsoon Intervals' (green shading) observed in the composite Chinese speleothem δ^{18}O record (*15, 17*), whilst for TX and TXII the estimates are based on the results presented in this study (see Fig. 2, main text). The pink shading and red italicised numbers show the duration of each termination (in kyr) based on an assessment of when the termination was completed. For TI and TII, completion-age estimates are sourced from data presented in *ref. 63* and *ref. 64* respectively. For TIIIa to TVII, the age at the point where the first derivative of the LR04 benthic δ^{18}O series ($\Delta\delta^{18}O/\Delta T$) crosses the zero line was chosen – this was adjusted to account for the difference in termination commencement age between LR04 and the Chinese speleothem record. Note that when using the first derivative to determine the termination completion age, we ensured that this estimate was consistent with the approximate position of the termination completion from the LR04 δ^{18}O series (for example, for TV the $\Delta\delta^{18}O/\Delta T$ first crosses the zero line at 423 ka, but it is clear from the LR04 δ^{18}O that the termination has barely reached the half-way point).

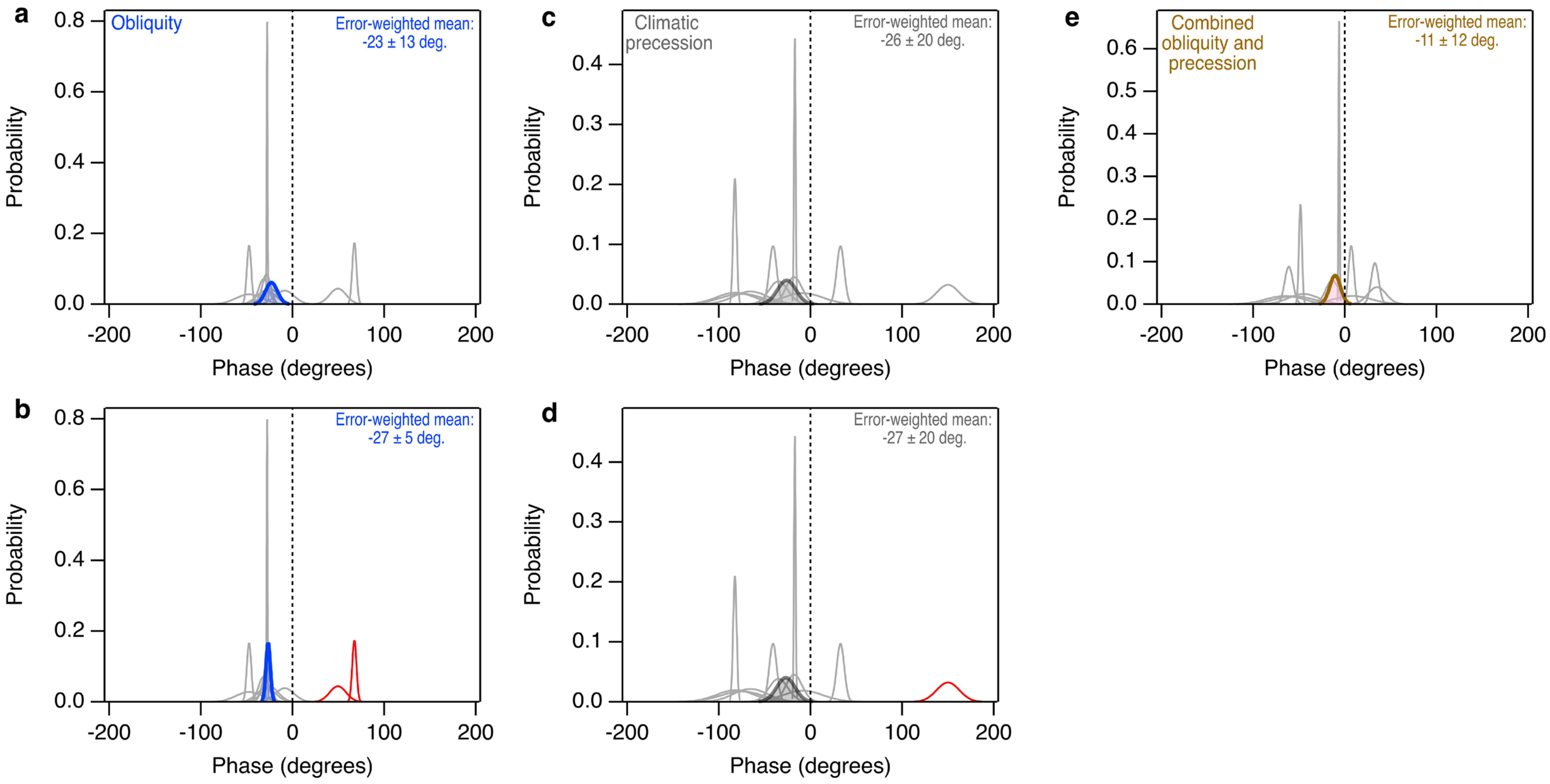

Fig. S8: Phase probability distributions for individual terminations (light grey) for obliquity (a, c), climatic precession (b, d) and an insolation forcing metric combining obliquity and climatic precession (e) (*13*). Phase uncertainties were calculated from the corresponding 95% age uncertainties (see SOM text). The error-weighted phase mean and 95% uncertainty from the individual distributions of each metric were calculated in *Isotoplot* (*65*) and represented by the heavy coloured curves (blue = obliquity, grey = climatic precession, brown = combined obliquity and precession). In (b) and (d), the phase means and uncertainties for obliquity and precession (respectively) are based on the removal of outliers (shown in red: two for obliquity, one for precession). Removal of these outliers, which are automatically detected in *Isotplot*, makes little difference to the means but halves the 95% uncertainty for obliquity. However, there is no reason to exclude outliers in the case of this study (see Materials and Methods). The heavy coloured curves from (a), (c) and (e) are superimposed in Figure 4c.

Table S1. U-Pb age data.

U-Pb dating results for isochron and single-aliquot analyses performed on CC8, CC30, CC119 and CC122 stalagmites.

Sample ID	Depth[¥] from top (mm) (100% uncert.)	Total Pb (ppb)	U (ppb)	$^{238}U/^{206}Pb$ (2σ error in %)	$^{207}Pb/^{206}Pb$ (2σ error in %)	MSWD[*]	$(^{234}U/^{238}U)_{measured}$ (±95% uncertainty)	**Age (Ma) corrected for $(^{234}U/^{238}U)_{initial}$ (±2σ error)**
Isochron analyses								
CC8-3[§]	385.6 (4.0)					227	0.9788 (0.0015)	0.874 (0.019)
CC8-3-1		2.29	7857	6060.97 (0.53)	0.323 (0.931)			
CC8-3-2		2.35	7489	5836.35 (0.29)	0.343 (0.424)			
CC8-3-3		1.54	7103	7011.64 (0.54)	0.247 (1.400)			
CC8-3-4		1.60	6965	6827.80 (0.57)	0.260 (1.350)			
CC8-3-5		2.14	7653	6203.86 (0.41)	0.314 (0.739)			
CC8-3-6		2.69	7469	5385.32 (0.36)	0.375 (0.482)			
CC119-1	447.0 (5.0)					0.94	0.9722 (0.0018)	0.887 (0.013)
CC119-1-1		2.68	4698	4196.47 (3.07)	0.484 (2.701)			
CC119-1-3		4.62	4870	2819.72 (1.12)	0.592 (0.597)			
CC119-1-5		5.37	4969	2541.47 (1.10)	0.614 (0.526)			
CC119-1-6		7.79	5110	1899.71 (0.73)	0.665 (0.268)			
CC119-1-9		9.66	5016	1547.79 (0.61)	0.692 (0.190)			
CC119-1-12		0.87	4590	7946.35 (5.16)	0.186 (20.032)			
CC119-2	457.9 (5.0)					0.48	0.9708 (0.0017)	0.893 (0.015)
CC119-2-2		5.17	4800	2569.91 (2.07)	0.610 (1.010)			
CC119-2-4		5.05	5017	2695.93 (1.37)	0.601 (0.702)			
CC119-2-7		5.47	5285	2635.16 (1.31)	0.607 (0.652)			
CC119-2-10		4.06	5419	3391.08 (1.45)	0.547 (0.958)			
CC119-2-12		2.90	5465	4397.10 (2.65)	0.468 (2.490)			
CC119-2-14		2.02	5055	5327.28 (3.73)	0.395 (4.849)			
CC119-3	491.3 (5.0)					0.15	0.9743 (0.0016)	**0.894 (0.011)**
CC119-3-2		2.12	8442	6758.46 (2.72)	0.270 (6.427)			
CC119-3-4		4.23	8724	4581.01 (1.60)	0.446 (1.663)			
CC119-3-6		5.80	7538	3300.15 (1.32)	0.549 (0.866)			
CC119-3-8		5.06	7338	3580.97 (1.26)	0.526 (0.918)			
CC119-3-11		3.09	8801	5618.58 (2.20)	0.363 (3.306)			
CC119-4	549 (5.0)					0.66	0.9741 (0.0016)	**0.907 (0.012)**
CC119-4-1		0.80	5477	8776.15 (6.39)	0.100 (51.873)			
CC119-4-3		1.10	6025	7845.43 (3.88)	0.176 (16.178)			
CC119-4-5		3.93	6475	3931.95 (1.86)	0.494 (1.562)			
CC119-4-8		8.38	6153	2089.66 (1.37)	0.642 (0.567)			
CC119-4-12		10.19	5605	1622.55 (0.85)	0.680 (0.285)			

Sample ID	Depth from top (mm) (100% uncert.)	Total Pb (ppb)	U (ppb)	^{238}U/^{206}Pb (2σ error in %)	^{207}Pb/^{206}Pb (2σ error in %)	MSWD*	(^{234}U/^{238}U)$_{\text{measured}}$ (±95% uncertainty)	**Age (Ma) corrected for (^{234}U/^{238}U)$_{\text{initial}}$ (±2σ error)**
Isochron analyses (continued)								
CC119-6	695.2 (5.0)					3.6	0.9756 (0.0016)	**0.934 (0.013)**
CC119-6-2		2.41	5361	4781.96 (2.74)	0.412 (3.300)			
CC119-6-4		32.67	4554	449.91 (0.28)	0.775 (0.057)			
CC119-6-6		47.81	4099	281.01 (0.21)	0.790 (0.027)			
CC119-6-8		42.49	4158	319.80 (0.24)	0.786 (0.033)			
CC119-6-10		19.69	4830	775.56 (0.71)	0.748 (0.152)			
CC119-6-12		5.79	5286	2489.53 (1.58)	0.602 (0.801)			
CC122-1	700.2 (5.0)					1.4	0.9773 (0.0019)	**0.932 (0.014)**
CC122-1-2		1.78	4511	5165.31 (3.35)	0.376 (4.685)			
CC122-1-4		1.82	5083	5472.11 (2.85)	0.351 (4.530)			
CC122-1-5		2.56	5246	4517.17 (2.51)	0.431 (2.770)			
CC122-1-6		2.59	5205	4512.01 (3.42)	0.432 (3.780)			
CC122-1-8		1.59	5261	5988.35 (2.68)	0.308 (5.241)			
CC122-1-10		1.44	5395	6446.17 (3.67)	0.268 (8.777)			
CC122-1-12		1.48	5161	6243.92 (3.74)	0.289 (8.016)			
CC122-1-14		5.04	4337	2380.72 (1.61)	0.616 (0.763)			
CC122-4	732.3 (5.0)					0.43	0.9756 (0.0019)	**0.949 (0.016)**
CC122-4-1		1.74	6120	6147.11 (2.50)	0.289 (5.347)			
CC122-4-3		9.29	7798	2299.84 (0.66)	0.617 (0.312)			
CC122-4-6		9.85	7484	2125.97 (1.04)	0.632 (0.458)			
CC122-4-8		10.02	7466	2089.48 (0.90)	0.635 (0.387)			
CC122-4-10		3.61	7290	4441.63 (1.96)	0.435 (2.137)			
CC122-4-12		2.13	5619	5308.06 (3.56)	0.360 (5.430)			
CC122-2	749.6 (5.0)					10	0.9775 (0.0014)	**0.915 (0.090)**
CC122-2-2		16.15	5391	1028.52 (0.57)	0.724 (0.147)			
CC122-2-4		19.58	5298	845.46 (0.43)	0.740 (0.096)			
CC122-2-6		16.62	5180	964.40 (0.47)	0.730 (0.112)			
CC122-2-8		16.00	4924	954.46 (0.60)	0.730 (0.145)			
CC122-2-10		13.88	4817	1063.97 (0.53)	0.720 (0.141)			
CC122-2-12		15.04	4782	983.80 (0.65)	0.728 (0.158)			
CC122-2-14		18.39	4724	804.31 (0.43)	0.741 (0.095)			
CC122-2-16		15.28	4723	958.14 (0.51)	0.731 (0.124)			

Sample ID	Depth from top (mm) (100% uncert.)	Total Pb (ppb)	U (ppb)	^{238}U/^{206}Pb (2σ error in %)	^{207}Pb/^{206}Pb (2σ error in %)	MSWD*	(^{234}U/^{238}U)$_{\mathrm{measured}}$ (±95% uncertainty)	**Age (Ma) corrected for (^{234}U/^{238}U)$_{\mathrm{initial}}$ (±2σ error)**
Isochron analyses (continued)								
CC122-5	751.3 (5.0)					5	0.9785 (0.0016)	**0.948 (0.037)**
CC122-5-2		4.50	6720	3625.62 (2.62)	0.498 (2.159)			
CC122-5-3		5.98	6554	2873.07 (1.82)	0.567 (1.098)			
CC122-5-5		4.18	6790	3814.85 (1.78)	0.483 (1.573)			
CC122-5-6		6.38	6890	2799.26 (0.94)	0.569 (0.556)			
CC122-5-7		6.40	7106	2862.17 (0.86)	0.565 (0.519)			
CC122-5-9		7.49	7307	2602.10 (1.38)	0.587 (0.753)			
CC122-6	792.1 (5.0)					0.37	0.9780 (0.0019)	**0.958 (0.016)**
CC122-6-2		2.74	7589	5354.55 (2.78)	0.344 (4.570)			
CC122-6-5		4.22	8515	4352.59 (1.10)	0.432 (1.208)			
CC122-6-9		20.94	8309	1196.49 (0.39)	0.706 (0.110)			
CC122-6-11		11.96	8783	2044.34 (0.54)	0.633 (0.230)			
CC122-6-14		2.87	7526	5164.95 (2.10)	0.362 (3.182)			
CC122-7	804.7 (5.0)					1.3	0.9784 (0.0015)	**0.961 (0.012)**
CC122-7-2		2.60	7559	5459.44 (2.01)	0.334 (3.452)			
CC122-7-4		2.50	7544	5540.20 (1.67)	0.326 (2.989)			
CC122-7-7		1.38	8693	7746.63 (2.19)	0.133 (12.709)			
CC122-7-10		1.25	8007	7781.12 (1.91)	0.131 (11.364)			
CC122-7-13		1.91	6786	6102.31 (2.65)	0.280 (5.958)			
CC122-3	845.6 (5.0)					1.5	0.9777 (0.0011)	**0.978 (0.014)**
CC122-3-2		0.88	5185	7766.37 (5.24)	0.122 (33.763)			
CC122-3-4		1.38	6358	6910.68 (3.28)	0.202 (11.491)			
CC122-3-5		1.84	7474	6442.05 (2.07)	0.243 (5.655)			
CC122-3-6		1.85	7459	6426.64 (2.17)	0.245 (5.896)			
CC122-3-8		1.89	6912	6103.51 (2.01)	0.271 (4.719)			
CC122-3-9		1.71	6282	6165.42 (2.31)	0.269 (5.512)			
CC122-3-10		1.55	5991	6315.85 (2.66)	0.253 (6.897)			
CC122-3-11		1.33	5656	6663.19 (3.67)	0.221 (11.431)			

Sample ID	Depth from top (mm) (100% uncert.)	Total Pb (ppb)	U (ppb)	^{238}U/^{206}Pb (2σ error in %)	^{207}Pb/^{206}Pb (2σ error in %)	MSWD*	(^{234}U/^{238}U)$_{measured}$ (±95% uncertainty)	**Age (Ma) corrected for (^{234}U/^{238}U)$_{initial}$ (±2σ error)**
					Single-aliquot analyses			
CC8-101[†]	13.0 (1.5)	2.38	7324	6034.62 (1.75)	0.363 (2.525)	n.a.	0.9779 (0.0025)	**0.810 (0.011)**
CC8-20	31.0 (3.0)	5.01	6390	3266.91 (0.73)	0.568 (0.444)	n.a.	0.9791 (0.0015)	**0.811 (0.012)**
CC8-103	40.5 (1.5)	2.87	10930	6747.02 (1.90)	0.304 (3.655)	n.a.	0.9786 (0.0026)	**0.817 (0.012)**
CC8-19	60.5 (2.0)	3.72	13752	6550.50 (0.33)	0.325 (0.517)	n.a.	0.9772 (0.0024)	**0.811 (0.010)**
CC8-105	66.0 (1.5)	4.40	12310	5675.31 (1.48)	0.389 (1.854)	n.a.	0.9773 (0.0023)	**0.813 (0.012)**
CC8-18	87.5 (2.0)	2.06	11699	7968.13 (1.03)	0.210 (1.330)	n.a.	0.9792 (0.0018)	**0.816 (0.009)**
CC8-108	93.0 (1.5)	2.91	11961	6985.91 (1.68)	0.284 (3.524)	n.a.	0.9809 (0.0024)	**0.809 (0.011)**
CC8-17	106.5 (2.0)	3.72	11175	5834.31 (0.29)	0.379 (0.320)	n.a.	0.9751 (0.0014)	**0.820 (0.007)**
CC8-112	127.0 (1.5)	3.02	10131	6263.41 (1.32)	0.340 (2.031)	n.a.	0.9794 (0.0027)	**0.813 (0.012)**
CC8-114	147.0 (1.5)	2.71	10199	6679.37 (1.97)	0.304 (3.784)	n.a.	0.9809 (0.0023)	**0.814 (0.011)**
CC8-116	195.0 (1.5)	1.82	10210	7975.50 (1.77)	0.196 (6.124)	n.a.	0.9771 (0.0024)	**0.843 (0.012)**
CC8-14	207.0 (2.0)	3.91	9509	5083.88 (0.29)	0.423 (0.306)	n.a.	0.9775 (0.0017)	**0.836 (0.009)**
CC8-119	224.0 (1.5)	3.66	9879	5471.18 (1.03)	0.394 (1.164)	n.a.	0.9801 (0.0023)	**0.823 (0.011)**
CC8-124	271.0 (1.5)	3.06	9957	6088.87 (1.36)	0.340 (2.103)	n.a.	0.9801 (0.0023)	**0.833 (0.012)**
CC8-126	286.0 (1.5)	3.20	8711	5531.82 (1.94)	0.385 (2.542)	n.a.	0.9808 (0.0024)	**0.828 (0.011)**
CC30-2	302.6 (5.0)	0.85	6994	9183.65 (4.04)	0.075 (44.864)	n.a.	0.9857 (0.0024)	**0.838 (0.012)**
CC8-128	314.0 (1.5)	3.77	9183	5138.16 (1.56)	0.413 (1.768)	n.a.	0.9794 (0.0023)	**0.839 (0.013)**
CC30-3	319.5 (5.0)	0.84	5855	8727.72 (4.78)	0.110 (34.624)	n.a.	0.9856 (0.0024)	**0.840 (0.012)**
CC8-130	325.0 (1.5)	3.66	9667	5432.80 (2.31)	0.387 (3.042)	n.a.	0.9804 (0.0023)	**0.841 (0.013)**
CC30-4	335.1 (5.0)	0.80	7546	9446.60 (2.56)	0.055 (38.547)	n.a.	0.9855 (0.0024)	**0.837 (0.012)**
CC30-6	345.8 (5.0)	5.45	8812	3898.75 (2.26)	0.498 (1.817)	n.a.	0.9863 (0.0024)	**0.841 (0.014)**
CC30-1-1	349.9 (5.0)	0.72	6145	9113.62 (3.37)	0.068 (40.947)	n.a.	0.9874 (0.0024)	**0.844 (0.011)**
CC30-8	350.4 (5.0)	3.99	8015	4492.84 (1.62)	0.447 (1.588)	n.a.	0.9879 (0.0025)	**0.840 (0.012)**
CC30-10	352.4 (5.0)	7.69	8690	2953.31 (1.14)	0.574 (0.605)	n.a.	0.9833 (0.0024)	**0.856 (0.017)**
CC30-12	353.9 (5.0)	3.04	8619	5551.27 (2.04)	0.358 (3.047)	n.a.	0.9868 (0.0025)	**0.849 (0.013)**
CC30-2-12	357.1 (5.0)	1.24	6467	7703.26 (4.64)	0.180 (18.613)	n.a.	0.9840 (0.0035)	**0.863 (0.018)**
CC8-64	402.1 (2.5)	1.92	5372	5684.76 (4.81)	0.351 (7.637)	n.a.	0.9799 (0.0014)	**0.875 (0.013)**

Sample ID	Depth from top (mm) (100% uncert.)	Total Pb (ppb)	U (ppb)	^{238}U/^{206}Pb (2σ error in %)	^{207}Pb/^{206}Pb (2σ error in %)	MSWD*	(^{234}U/^{238}U)$_{measured}$ (±95% uncertainty)	**Age (Ma) corrected for (^{234}U/^{238}U)$_{initial}$ (±2σ error)**
Single-aliquot analyses (continued)								
CC8-63	411.6 (2.5)	0.89	6321	8591.53 (2.86)	0.116 (19.461)	n.a.	0.9790 (0.0016)	**0.877 (0.010)**
CC8-62	416.6 (2.5)	1.57	7202	7109.84 (2.64)	0.227 (7.950)	n.a.	0.9822 (0.0018)	**0.876 (0.010)**
CC8-87	424.6 (1.0)	7.02	3495	4575.96 (3.70)	0.440 (3.957)	n.a.	0.9807 (0.0013)	**0.872 (0.013)**
CC8-61	424.6 (2.5)	1.55	6709	7026.30 (3.44)	0.239 (9.605)	n.a.	0.9816 (0.0014)	**0.869 (0.009)**
CC8-21	428.6 (2.0)	3.05	9329	5676.34 (0.45)	0.351 (0.688)	n.a.	0.9816 (0.0018)	**0.868 (0.010)**
CC8-60	431.6 (2.5)	2.06	7084	6139.49 (1.35)	0.313 (2.565)	n.a.	0.9810 (0.0013)	**0.871 (0.007)**
CC8-59^{O}	435.6 (2.5)	2.7	6881	5187.30 (1.47)	0.389 (1.963)	n.a.	0.9832 (0.0012)	**0.863 (0.008)**
CC8-58	437.6 (2.5)	1.17	6235	7578.41 (2.09)	0.191 (7.855)	n.a.	0.9803 (0.0021)	**0.881 (0.012)**
CC8-86	444.6 (1.0)	2.14	4899	5207.73 (8.89)	0.386 (12.059)	n.a.	0.9820 (0.0020)	**0.872 (0.022)**
CC8-31	446.6 (2.5)	1.43	5956	6520.20 (2.24)	0.273 (4.960)	n.a.	0.9830 (0.0018)	**0.875 (0.010)**
CC119-15^{R}	451.7 (5.0)	10.03	5993	1753.90 (0.81)	0.677 (0.277)	n.a.	0.9714 (0.0016)	**0.884 (0.033)**
CC8-85	452.6 (1.5)	1.98	5877	5859.68 (6.58)	0.312 (12.625)	n.a.	0.9853 (0.0012)	**0.893 (0.015)**
CC8-12	456.1 (2.0)	1.85	5934	5734.93 (0.70)	0.330 (1.200)	n.a.	0.9841 (0.0019)	**0.885 (0.010)**
CC119-16	457.0 (5.0)	4.8	6159	3309.01 (1.67)	0.556 (1.059)	n.a.	0.9712 (0.0016)	**0.881 (0.017)**
CC119-9^{O}	469.7 (5.0)	2.51	3239	3304.94 (2.34)	0.542 (1.580)	n.a.	0.9727 (0.0030)	**0.929 (0.028)**
CC8-11	478.1 (2.0)	2.97	6912	4750.37 (0.35)	0.406 (0.402)	n.a.	0.9850 (0.0015)	**0.895 (0.009)**
CC119-17	494.2 (5.0)	2.13	7785	6450.2 (2.09)	0.299 (4.258)	n.a.	0.9741 (0.0016)	**0.889 (0.011)**
CC8-32	497.6 (2.0)	2.53	7631	5527.61 (0.89)	0.342 (1.460)	n.a.	0.9849 (0.0012)	**0.891 (0.007)**
CC119-18	513.2 (5.0)	8.46	8242	2633.94 (0.94)	0.603 (0.475)	n.a.	0.9739 (0.0017)	**0.892 (0.021)**
CC8-10	521.6 (2.0)	3.42	7343	4493.98 (0.31)	0.423 (0.330)	n.a.	0.9869 (0.0024)	**0.898 (0.013)**
CC8-27	538.1 (3.5)	1.1	6124	7328.15 (1.21)	0.180 (4.860)	n.a.	0.9850 (0.0014)	**0.903 (0.008)**
CC119-19^{R}	554.4 (5.0)	10.17	5729	1654.79 (0.67)	0.678 (0.228)	n.a.	0.9766 (0.0019)	**0.898 (0.032)**
CC8-33^{O}	555.6 (2.0)	2.33	5101	4575.82 (0.73)	0.425 (0.821)	n.a.	0.9844 (0.0019)	**0.889 (0.011)**
CC8-91	561.1 (2.0)	2.8	7769	5460.20 (3.40)	0.346 (5.529)	n.a.	0.9821 (0.0010)	**0.910 (0.010)**
CC119-20	561.8 (5.0)	0.96	4776	7514.34 (3.77)	0.200 (13.390)	n.a.	0.9734 (0.0018)	**0.919 (0.015)**
CC8-34	565.1 (2.0)	3.37	7726	4732.16 (0.44)	0.415 (0.512)	n.a.	0.9803 (0.0018)	**0.904 (0.012)**
CC8-9	574.6 (2.0)	2.07	6653	5711.02 (0.34)	0.325 (0.344)	n.a.	0.9831 (0.0020)	**0.903 (0.012)**
CC119-11	584.7 (5.0)	2.15	6222	5661.74 (3.02)	0.348 (4.860)	n.a.	0.9754 (0.0018)	**0.911 (0.014)**

Sample ID	Depth from top (mm) (100% uncert.)	Total Pb (ppb)	U (ppb)	^{238}U/^{206}Pb (2σ error in %)	^{207}Pb/^{206}Pb (2σ error in %)	MSWD*	(^{234}U/^{238}U)$_{measured}$ (±95% uncertainty)	**Age (Ma) corrected for (^{234}U/^{238}U)$_{initial}$ (±2σ error)**
CC8-29	605.1 (2.0)	5.88	8061	3342.69 (0.44)	0.527 (0.327)	n.a.	0.9837 (0.0010)	**0.902 (0.012)**
CC119-21	606.7 (5.0)	2.68	7236	5388.43 (1.64)	0.376 (2.327)	n.a.	0.9749 (0.0016)	**0.902 (0.012)**
CC8-70	632.1 (2.5)	1.82	6908	6354.81 (2.02)	0.270 (4.763)	n.a.	0.9824 (0.0014)	**0.907 (0.009)**
CC8-90	634.6 (1.5)	1.36	7045	7664.03 (7.38)	0.150 (37.392)	n.a.	0.9825 (0.0011)	**0.919 (0.013)**
CC8-69	636.1 (2.5)	1.83	6723	6230.14 (1.69)	0.280 (3.802)	n.a.	0.9815 (0.0017)	**0.914 (0.011)**
CC8-35	637.6 (2.0)	1.55	5412	5934.37 (1.40)	0.304 (2.790)	n.a.	0.9832 (0.0013)	**0.907 (0.009)**
CC8-8	640.6 (2.0)	0.8	5972	8130.74 (0.55)	0.112 (3.780)	n.a.	0.9813 (0.0022)	**0.923 (0.014)**
CC8-68	646.1 (2.5)	1.38	5270	6439.73 (3.77)	0.256 (9.625)	n.a.	0.9829 (0.0014)	**0.916 (0.011)**
CC8-67	650.1 (2.5)	2.19	4989	4778.54 (2.21)	0.398 (2.838)	n.a.	0.9824 (0.0017)	**0.923 (0.013)**
CC119-22	652.7 (7.0)	5.05	7862	3727.57 (0.92)	0.508 (0.726)	n.a.	0.9748 (0.0020)	**0.912 (0.017)**
CC119-5	652.9 (7.0)	1.52	6775	7064.90 (3.11)	0.230 (9.143)	n.a.	0.9749 (0.0019)	**0.919 (0.015)**
CC119-12^{R}	660.1 (7.0)	29.16	5527	605.69 (0.30)	0.763 (0.054)	n.a.	0.9738 (0.0020)	**0.938 (0.108)**
CC8-66	663.6 (2.5)	2.04	5229	5106.22 (2.72)	0.357 (4.202)	n.a.	0.9854 (0.0014)	**0.931 (0.011)**
CC8-28^{R}	666.6 (2.0)	4.79	4061	2290.74 (0.42)	0.612 (0.218)	n.a.	0.9849 (0.0025)	**0.919 (0.022)**
CC8-65	667.6 (2.5)	1.14	4600	6538.01 (3.69)	0.233 (10.698)	n.a.	0.9836 (0.0018)	**0.936 (0.014)**
CC119-23^{R}	674.3 (7.0)	11.99	7135	1729.74 (0.56)	0.671 (0.197)	n.a.	0.9748 (0.0016)	**0.920 (0.031)**
CC119-24^{R}	682.2 (5.0)	17.46	5819	1027.67 (0.38)	0.727 (0.094)	n.a.	0.9757 (0.0014)	**0.930 (0.057)**
CC8-79	686.6 (1.5)	1.38	5129	6353.80 (6.24)	0.232 (18.218)	n.a.	0.9874 (0.0014)	**0.943 (0.014)**
CC119-25	693.8 (5.0)	4.18	5768	3421.23 (1.50)	0.527 (1.082)	n.a.	0.9754 (0.0019)	**0.931 (0.020)**
CC122-15^{R}	699.3 (5.0)	18.4	6762	1123.09 (0.40)	0.719 (0.106)	n.a.	0.9760 (0.0015)	**0.935 (0.052)**
CC122-16^{R}	704.5 (5.0)	10.24	6410	1818.96 (1.51)	0.659 (0.571)	n.a.	0.9753 (0.0019)	**0.947 (0.033)**
CC119-13^{R}	707.4 (5.0)	25.47	6412	791.91 (0.41)	0.746 (0.088)	n.a.	0.9746 (0.0019)	**0.950 (0.082)**
CC122-8^{R}	717.6 (5.0)	11.57	7201	1794.34 (0.73)	0.661 (0.274)	n.a.	0.9755 (0.0017)	**0.946 (0.034)**
CC8-38	719.6 (2.5)	2.49	5651	4676.79 (2.72)	0.382 (3.752)	n.a.	0.9889 (0.0021)	**0.941 (0.015)**
CC122-17^{R}	736.9 (5.0)	11.6	5147	1335.02 (0.80)	0.699 (0.239)	n.a.	0.9763 (0.0016)	**0.951 (0.043)**
CC122-18	755.0 (5.0)	7.3	7032	2565.03 (0.78)	0.592 (0.414)	n.a.	0.9770 (0.0016)	**0.952 (0.022)**
CC8-40	759.6 (2.5)	4.63	4595	3651.10 (1.58)	0.485 (0.992)	n.a.	0.9844 (0.0017)	**0.946 (0.014)**
CC122-9^{R}	765.8 (5.0)	22.38	7157	986.09 (0.40)	0.727 (0.097)	n.a.	0.9763 (0.0025)	**0.979 (0.068)**
CC122-19^{R}	773.9 (5.0)	9.04	7390	2242.67 (0.70)	0.619 (0.326)	n.a.	0.9766 (0.0016)	**0.964 (0.027)**
CC8-75	774.6 (1.5)	2.93	4922	3953.69 (4.80)	0.453 (4.839)	n.a.	0.9870 (0.0019)	**0.942 (0.018)**

Sample ID	Depth from top (mm) (100% uncert.)	Total Pb (ppb)	U (ppb)	^{238}U/^{206}Pb (2σ error in %)	^{207}Pb/^{206}Pb (2σ error in %)	MSWD[*]	(^{234}U/^{238}U)$_{measured}$ (±95% uncertainty)	**Age (Ma) corrected for (^{234}U/^{238}U)$_{initial}$ (±2σ error)**
CC122-10[R]	782.5 (5.0)	9.99	7764	2145.99 (0.58)	0.625 (0.263)	n.a.	0.9770 (0.0017)	**0.975 (0.029)**
CC8-74	785.6 (2.0)	4.98	4815	2567.49 (1.69)	0.580 (0.961)	n.a.	0.9863 (0.0022)	**0.943 (0.021)**
CC8-6	791.6 (2.0)	1.38	4454	5471.66 (0.87)	0.298 (1.770)	n.a.	0.9887 (0.0011)	**0.962 (0.008)**
CC122-20[R]	793.7 (5.0)	12.53	7109	1643.56 (0.64)	0.667 (0.228)	n.a.	0.9751 (0.0016)	**1.015 (0.042)**
CC8-57	794.1 (2.5)	1.55	5677	5983.79 (2.25)	0.253 (5.820)	n.a.	0.9896 (0.0019)	**0.950 (0.013)**
CC122-21	796.0 (5.0)	3	7592	5055.91 (2.23)	0.371 (3.233)	n.a.	0.9792 (0.0029)	**0.953 (0.023)**
CC8-54	798.6 (2.5)	1.61	5652	5400.31 (1.66)	0.307 (3.251)	n.a.	0.9884 (0.0022)	**0.960 (0.014)**
CC8-42	799.6 (2.0)	2.19	5708	4880.67 (0.96)	0.355 (1.490)	n.a.	0.9885 (0.0017)	**0.960 (0.012)**
CC122-12[R]	799.6 (5.0)	14.81	8091	1586.74 (0.47)	0.671 (0.162)	n.a.	0.9757 (0.0018)	**1.018 (0.044)**
CC8-73	801.1 (2.0)	2.77	6072	4648.23 (5.22)	0.375 (7.428)	n.a.	0.9875 (0.0016)	**0.971 (0.017)**
CC8-53	802.6 (2.5)	1.34	5473	6277.53 (1.90)	0.227 (5.708)	n.a.	0.9891 (0.0021)	**0.952 (0.013)**
CC122-22	802.9 (5.0)	1.79	8035	6793.83 (2.24)	0.218 (7.061)	n.a.	0.9781 (0.0028)	**0.961 (0.024)**
CC8-72	811.6 (1.5)	2.27	6022	5235.76 (6.51)	0.313 (12.425)	n.a.	0.9906 (0.0017)	**0.965 (0.017)**
CC8-71	817.6 (1.5)	2.67	5046	4165.55 (3.33)	0.421 (3.859)	n.a.	0.9879 (0.0019)	**0.968 (0.016)**
CC8-56	821.1 (2.5)	2.17	4705	4487.73 (2.53)	0.387 (3.424)	n.a.	0.9892 (0.0010)	**0.968 (0.010)**
CC8-43	826.1 (2.5)	4.05	6109	6137.32 (1.79)	0.230 (4.500)	n.a.	0.9912 (0.0014)	**0.957 (0.009)**
CC8-5	832.1 (2.0)	1.76	5427	5534.28 (4.02)	0.285 (8.790)	n.a.	0.9908 (0.0012)	**0.962 (0.011)**
CC8-52	836.6 (2.5)	1.46	6094	6353.26 (3.41)	0.206 (11.650)	n.a.	0.9900 (0.0016)	**0.968 (0.011)**
CC8-51	840.1 (2.5)	1.27	5983	6617.00 (2.36)	0.184 (9.333)	n.a.	0.9899 (0.0012)	**0.964 (0.009)**
CC122-24[R]	854.6 (5.0)	12.64	8155	1835.31 (0.90)	0.647 (0.360)	n.a.	0.9775 (0.0016)	**1.007 (0.034)**
CC122-14[R]	858.6 (5.0)	10.19	8246	2216.07 (0.97)	0.613 (0.466)	n.a.	0.9784 (0.0019)	**0.994 (0.028)**

Notes:

[¥] Age-sample depths are given on the composite depth scale.

[*] MSWD = mean square weighted deviation, calculated by *Isoplot* (*65*) based upon the assumptions of a model 1 or 2 fit.

[§] Only one new isochron age for CC8 is presented here; the other seven isochron ages were presented in ref. *22*.

[†] Ages for stalagmite CC8 below the composite depth position of 402.1 mm (i.e. those older than and including CC8-64) were originally published in ref. *19* and have been corrected using a revised estimate of the common Pb composition based on subsequent dating (see fig. S3). A revised age for sample CC8-7 from *ref. 22* is not provided here due to subsequent detection of analytical problems.

[O] Rejected as outlier (shown in grey).

[R] Rejected due to low-radiogenic composition of the sample (^{238}U/^{206}Pb < 2500) (shown in grey).

Table S2. Comparison of sedimentation rates for Site U1385. Data are derived from previously published age models (*30*) and the age models generated from this study. The 'DH2015 Oxy' is based on tuning to the LR04 benthic stack; 'DH2015 Orbital' is based on tuning the sediment lightness series to orbital precession; 'DH2015 GLSyn' is based on tuning to the Greenland synthetic time series (*66*); and 'DH2015 ^{14}C' is based on radiocarbon ages. The minimum rates shown for all DH models except DH2015 ^{14}C exclude a section through late MIS12 to early MIS11 where a hiatus is suspected - see *ref. 30*. For the models generated from this study, 'CC-Raw' is an interpolation of the Corchia U-Pb age model through the 80 age-control points, and is free of any sedimentation rate constraints; the 'CC-Bacon' is produced from the *Bacon for R* software (*56*) and used a mean sedimentation rate constraint of 0.1 m kyr^{-1}; and 'CC-FGR' is calculated using the finite growth-rate age modelling procedure used in the Corchia U-Pb age model with growth rate allowed to vary by a factor of ± 3. The '% difference' is the percentage difference of the age offset between CC-Raw and CC-Bacon, or CC-Raw and CC-FGR, and the corresponding error envelope for CC-Raw. Note also that the age uncertainties for both the CC-Bacon and CC-FGR models are not used to provide the final age uncertainty estimates for the start of both terminations because the input uncertainties from the CC-1385 tie points are correlated and cannot be considered independently as assumed by these models.

	DH2015 Oxy[†]	**DH2015 Orbital[†]**	**DH2015 GLSyn[#]**	**DH2015 ^{14}C[§]**	**CC-Raw[¥]**	**CC-Bacon for R[¥]**	**CC-FGR[¥]**
Sedimentation rate (m kyr^{-1})							
Minimum	0.03	0.06	0.04	0.13	0.02	0.04	0.03
Maximum	0.26	0.22	0.33	0.35	0.86	0.29	0.26
Mean	0.12	0.12	0.13	0.20	0.15	0.11	0.12
Termination age (ka) ±2σ							
Start of TX[&]	874.3	873.9	n.a.	n.a.	875.4 +2.9/-4.3	876.3 +1.9/-2.0	875.7 +2.1/-1.8
Start of TX[*]					875.4 ± 4.7	876.3 ± 2.8	875.7 ± 2.9
% difference[‡]	n.a.	n.a.	n.a.	n.a.		12.4	3.4
Start of TXII[&]	961.5	962.0	n.a.	n.a.	960.1 + 4.3/- 3.0	960.1 +1.8/-1.7	960.7 +1.4/-1.1
Start of TXII[*]					960.1 ± 4.7	960.1 ± 2.7	960.7 ± 2.4
% difference[‡]	n.a.	n.a.	n.a.	n.a.	n.a.	0.5	8.4

Notes:
† Based on an age model for the entire core depth (*30*)
# Based on an age model for the period 0-800 ka (*30, 66*)
§ Based on an age model for the period 0-28 ka (*30*)
¥ From this study
& Uncertainty estimate based on age modelling only
* Age-modelling and synchronization uncertainties combined in quadrature
‡ Difference between the CC-Raw and CC-Bacon or CC-FGR ages as a percentage of the CC-Raw age-uncertainty envelope (excludes the synchronization uncertainty)

Table S3. LR04 benthic $\delta^{18}O$ marker points used to identifying the start and end of Terminations IIIa to VII. The starting points were chosen based on their alignment with the ODP980 (TIIIa to TIV) (*61*) and U1314 (TV to TVII) (*62*) benthic $\delta^{18}O$ values that mark the start of each terminal Heinrich event (see Materials and Methods). The ages shown here are the unadjusted ages based on two different LR04 age models: the original (*5*) and a depth-derived model (*13*). (NB: the corresponding ages for TI and TII are direct radiometric estimates from *ref. 63* and *ref. 64*, respectively; ages for TX and TXII are from this study.

Term. number	**LR04 benthic $\delta^{18}O$ value at start of termination**	**Original LR04 benthic age (ka)**	**Huybers (2011) LR04 benthic age (ka)**	**LR04 benthic $\delta^{18}O$ value at end of termination**	**Original LR04 benthic age (ka)**	**Huybers (2011) LR04 benthic age (ka)**
I	n.a.	n.a.	n.a.	n.a.	n.a.	n.a.
II	n.a.	n.a.	n.a.	n.a.	n.a.	n.a.
IIIa	4.410	222.5	211.2	3.505	216.5	205.6
III	4.540	250.5	237.8	3.440	239.5	226.9
IV	4.815	342.5	329.8	3.210	328.5	313.1
V	5.015	430.5	425.9	3.185	409.5	405.3
VI	4.485	537.5	539.6	3.945	530.5	535.2
VIIa	4.300	583.5	584.2	3.425	575.5	576.5
VII	4.955	627.0	625.9	3.525	613.0	613.1
X	n.a.	n.a.	n.a.	n.a.	n.a.	n.a.
XII	n.a.	n.a.	n.a.	n.a.	n.a.	n.a.

Table S4a. Termination timing and spacing, and the prevailing astronomical and insolation metrics (see Materials and Methods for explanation). The timing of the termination completions for TIIIa to TVII are based on the control points from the LR04 benthic δ^{18}O (Table S3); the remaining completion ages have been derived radiometrically (*63, 64*; this study). The TIIIa to TVII completion ages are based on the original LR04 age model (*5*) and have been adjusted according to the radiometric age estimates for the termination start. The 'Obl.' and 'Prec.' columns are derived by dividing the spacing in kyr by the nearest whole number of obliquity or precession cycles. The mean values shown in bold at the base of the table are the averages ± one standard deviation of these column values. For the phase lead (final column), 360º was added to the two values of obliquity that are beyond zero phase; values where termination onsets show a precession lead (i.e. negative) are italicised.

Term. number	**Termination age (ka) and duration (kyr)**				**Termination spacing at midpoint (kyr)**			**Astronomical metrics**						**Insolation metrics (at 65ºN)**						**Astronomical phasing (º)**						**Phase lead (obl. minus prec.) at start**
					Spac-ing	**Obl.**	**Prec.**	**Obliquity (º)**			**Precession index**			**Cal. sum. half-yr insol.**			**Integrated sum. insol.**			**Obliquity**			**Precession**			
	Start	*Mid*	*End*	*Dur.*				*Start*	*Mid*	*End*	*Start*	*Mid*	*End*	*Start*	*Mid*	*End*	*Start*	*Mid*	*End*	*Start*	*Mid*	*End*	*Start*	*Mid*	*End*	
I	18	12.5	7	11	120	40.0	24.0	23.48	24.13	24.16	0.006	-0.019	-0.006	5.84	6.03	5.99	5.04	5.20	5.18	282	332	23	249	343	77	33
II	136	132.5	129	7	85.5	42.8	21.4	23.97	24.23	24.21	0.027	-0.005	-0.036	5.84	6.00	6.10	5.09	5.19	5.25	313	346	19	225	278	330	88
IIIa	221	218	215	6	26.5		26.5	23.64	24.12	24.41	-0.048	-0.038	-0.003	6.04	6.09	6.03	5.18	5.24	5.22	284	313	341	344	33	82	*-59*
III	250	244.5	239	11	91.5	45.8	22.9	24.36	23.74	22.73	0.018	-0.029	-0.027	5.94	6.01	5.87	5.18	5.15	4.97	18	68	117	229	319	49	149
IV	343	336	329	14	84.5	42.3	21.1	23.26	24.18	24.07	0.018	-0.028	0.003	5.74	6.06	5.95	4.97	5.23	5.15	265	332	38	216	342	98	49
V	431	420.5	410	21	111	37.0	22.2	22.78	24.13	23.86	-0.005	0.011	-0.015	5.78	5.91	5.98	4.93	5.15	5.15	234	329	57	300	150	342	*-66*
VI	535	531.5	528	7	50.5	50.5	25.3	24.18	23.93	23.52	-0.004	-0.010	-0.014	6.00	5.98	5.94	5.19	5.15	5.09	18	50	81	290	325	0	88
VIIa	586	582	578	8	44	44.0	22.0	23.74	24.00	24.07	0.026	-0.023	-0.043	5.80	6.02	6.09	5.05	5.19	5.24	303	336	8	229	295	0	74
VII	633	626	619	14				23.19	23.74	23.84	0.021	-0.011	-0.025	5.73	5.93	6.02	4.96	5.12	5.16	246	18	27	180	36	54	66
X	875	870	865	10	88.5	44.5	22.3	23.61	23.75	23.68	0.037	-0.002	-0.038	5.72	5.90	6.03	5.00	5.10	5.16	309	351	31	196	278	0	112
XII	960	958.5	957	3				23.79	23.85	23.90	-0.050	-0.055	-0.050	6.05	6.09	6.09	5.21	5.23	5.23	319	331	344	327	352	18	*-8*
					Mean	**41±7**	**23±2**																			

Extended Data Table 4b. Same as for Table S4a except that the depth-derived age model of *ref. 13* is used for TIIIa to TVII instead of the original LR04 age model (*5*).

Term. number	**Termination age (ka) and duration (kyr)**				**Termination spacing at midpoint (kyr)**			**Astronomical metrics**						**Insolation metrics (at 65ºN)**						**Astronomical phasing (º)**					
					Spac-ing	**Obl.**	**Prec.**	**Obliquity (º)**			**Precession index**			**Cal. sum. half-yr insol.**			**Integrated sum. insol.**			**Obliquity**			**Precession**		
	Start	*Mid*	*End*	*Dur.*				*Start*	*Mid*	*End*	*Start*	*Mid*	*End*	*Start*	*Mid*	*End*	*Start*	*Mid*	*End*	*Start*	*Mid*	*End*	*Start*	*Mid*	*End*
I	18	12.5	7	11	120	40.0	24.0	23.48	24.13	24.16	0.010	-0.019	-0.006	5.84	6.03	5.99	5.04	5.20	5.18	282	332	23	249	343	77
II	136	132.5	129	7	85.7	42.9	21.4	23.97	24.23	24.21	0.030	-0.005	-0.036	5.84	6.00	6.10	5.09	5.19	5.25	313	346	19	225	278	330
IIIa	221	218.2	215.4	5.6	27.3	27.3	27.3	23.64	24.09	24.38	-0.050	-0.039	-0.008	6.04	6.09	6.04	5.18	5.24	5.23	284	311	337	344	30	75
III	250	245.5	239.1	10.9	89.2	44.6	22.3	24.36	23.74	22.75	0.020	-0.029	-0.028	5.94	6.01	5.87	5.18	5.15	4.98	18	68	116	229	319	48
IV	343	334.7	326.3	16.7	86	43.0	21.5	23.26	24.25	23.76	0.020	-0.030	0.025	5.74	6.08	5.81	4.97	5.25	5.05	265	344	38	216	5	98
V	431	420.7	410.3	20.7	112.5	37.5	22.5	22.78	24.12	23.89	0.000	0.011	-0.014	5.78	5.91	5.98	4.93	5.15	5.15	234	327	57	300	146	342
VI	535	533.4	530.6	4.4	49	49.0	24.5	24.18	24.04	23.83	0.000	-0.008	-0.012	6.00	5.98	5.97	5.19	5.17	5.14	18	38	58	290	312	334
VIIa	586	582.2	578.3	7.7	44.4	44.4	22.2	23.74	23.99	24.07	0.030	-0.021	-0.043	5.80	6.01	6.09	5.05	5.18	5.24	303	334	6	229	291	355
VII	633	626.6	620.2	12.8				23.19	23.70	23.87	0.020	-0.006	-0.031	5.73	5.91	6.04	4.96	5.10	5.18	246	327	45	180	308	90
X	875	869.5	864	10	89	44.5	22.3	23.61	23.75	23.68	0.037	-0.002	-0.038	5.72	5.90	6.03	5.00	5.10	5.16	309	351	31	196	278	0
XII	960	958.5	957	3				23.79	23.85	23.90	-0.050	-0.055	-0.050	6.05	6.09	6.09	5.21	5.23	5.23	319	331	344	327	352	18
					Mean	**41±7**	**23±2**																		

References and Notes

1. A. Berger, M. F. Loutre, Insolation values for the climate of the last 10 million years. *Quat. Sci. Rev.* **10**, 297–317 (1991). doi:10.1016/0277-3791(91)90033-Q

2. J. D. Hays, J. Imbrie, N. J. Shackleton, Variations in the Earth's orbit: Pacemaker of the ice ages. *Science* **194**, 1121–1132 (1976). doi:10.1126/science.194.4270.1121 Medline

3. N. G. Pisias, T. C. Moore Jr., The evolution of Pleistocene climate: A time series approach. *Earth Planet. Sci. Lett.* **52**, 450–458 (1981). doi:10.1016/0012-821X(81)90197-7

4. P. U. Clark, D. Archer, D. Pollard, J. D. Blum, J. A. Rial, V. Brovkin, A. C. Mix, N. G. Pisias, M. Roy, The middle Pleistocene transition: Characteristics, mechanisms, and implications for long-term changes in atmospheric pCO_2. *Quat. Sci. Rev.* **25**, 3150–3184 (2006). doi:10.1016/j.quascirev.2006.07.008

5. L. E. Lisiecki, M. E. Raymo, A Pliocene-Pleistocene stack of 57 globally distributed benthic $\delta^{18}O$ records. *Paleoceanogr. Paleoclimatol.* **20**, PA1003 (2005). doi:10.1029/2004PA001071

6. M. J. Head, P. L. Gibbard, Early-Middle Pleistocene transitions: Linking terrestrial and marine realms. *Quat. Int.* **389**, 7–46 (2015). doi:10.1016/j.quaint.2015.09.042

7. H. Elderfield, P. Ferretti, M. Greaves, S. Crowhurst, I. N. McCave, D. Hodell, A. M. Piotrowski, Evolution of ocean temperature and ice volume through the mid-Pleistocene climate transition. *Science* **337**, 704–709 (2012). doi:10.1126/science.1221294 Medline

8. L. D. Pena, S. L. Goldstein, Thermohaline circulation crisis and impacts during the mid-Pleistocene transition. *Science* **345**, 318–322 (2014). doi:10.1126/science.1249770 Medline

9. P. C. Tzedakis, M. Crucifix, T. Mitsui, E. W. Wolff, A simple rule to determine which insolation cycles lead to interglacials. *Nature* **542**, 427–432 (2017). doi:10.1038/nature21364 Medline

10. N. J. Shackleton, N. D. Opdyke, Oxygen-isotope and paleomagnetic stratigraphy of Pacific core V28-239 Late Pliocene to Latest Pleistocene. *Mem. Geol. Soc. Am.* **145**, 449–464 (1976). doi:10.1130/MEM145-p449

11. P. Huybers, C. Wunsch, Obliquity pacing of the late Pleistocene glacial terminations. *Nature* **434**, 491–494 (2005). doi:10.1038/nature03401 Medline

12. L. E. Lisiecki, Links between eccentricity forcing and the 100,000-year glacial cycle. *Nat. Geosci.* **3**, 349–352 (2010). doi:10.1038/ngeo828

13. P. Huybers, Combined obliquity and precession pacing of late Pleistocene deglaciations. *Nature* **480**, 229–232 (2011). doi:10.1038/nature10626 Medline

14. P. Huybers, Glacial variability over the last two million years: An extended depth-derived age model, continuous obliquity pacing, and the Pleistocene progression. *Quat. Sci. Rev.* **26**, 37–55 (2007). doi:10.1016/j.quascirev.2006.07.013

15. H. Cheng, R. L. Edwards, A. Sinha, C. Spötl, L. Yi, S. Chen, M. Kelly, G. Kathayat, X. Wang, X. Li, X. Kong, Y. Wang, Y. Ning, H. Zhang, The Asian monsoon over the past 640,000 years and ice age terminations. *Nature* **534**, 640–646 (2016). doi:10.1038/nature18591 Medline

16. P. Huybers, Early Pleistocene glacial cycles and the integrated summer insolation forcing. *Science* **313**, 508–511 (2006). doi:10.1126/science.1125249 Medline

17. H. Cheng, R. L. Edwards, W. S. Broecker, G. H. Denton, X. Kong, Y. Wang, R. Zhang, X. Wang, Ice age terminations. *Science* **326**, 248–252 (2009). doi:10.1126/science.1177840 Medline

18. See supplementary materials.

19. R. N. Drysdale, G. Zanchetta, J. C. Hellstrom, A. E. Fallick, J. Zhao, I. Isola, G. Bruschi, Palaeoclimatic implications of the growth history and stable isotope ($\delta^{18}O$ and $\delta^{13}C$) geochemistry of a Middle to Late Pleistocene stalagmite from central-western Italy. *Earth Planet. Sci. Lett.* **227**, 215–229 (2004). doi:10.1016/j.epsl.2004.09.010

20. P. Bajo, R. Drysdale, J. Woodhead, J. Hellstrom, G. Zanchetta, High-resolution U-Pb dating of an Early Pleistocene stalagmite from Corchia Cave (central Italy). *Quat. Geochronol.* **14**, 5–17 (2012). doi:10.1016/j.quageo.2012.10.005

21. J. Woodhead, J. Hellstrom, R. Maas, R. Drysdale, G. Zanchetta, P. Devine, E. Taylor, U-Pb geochronology of speleothems by MC-ICPMS. *Quat. Geochronol.* **1**, 208–221 (2006). doi:10.1016/j.quageo.2006.08.002

22. J. Woodhead, J. Hellstrom, R. Pickering, R. Drysdale, B. Paul, P. Bajo, U and Pb variability in older speleothems and strategies for their chronology. *Quat. Geochronol.* **14**, 105–113 (2012). doi:10.1016/j.quageo.2012.02.028

23. P. C. Tzedakis, R. N. Drysdale, V. Margari, L. C. Skinner, L. Menviel, R. H. Rhodes, A. S. Taschetto, D. A. Hodell, S. J. Crowhurst, J. C. Hellstrom, A. E. Fallick, J. O. Grimalt, J. F. McManus, B. Martrat, Z. Mokeddem, F. Parrenin, E. Regattieri, K. Roe, G. Zanchetta, Enhanced climate instability in the North Atlantic and southern Europe during the Last Interglacial. *Nat. Commun.* **9**, 4235 (2018). doi:10.1038/s41467-018-06683-3 Medline

24. B. Martrat, J. O. Grimalt, N. J. Shackleton, L. de Abreu, M. A. Hutterli, T. F. Stocker, Four climate cycles of recurring deep and surface water destabilizations on the Iberian margin. *Science* **317**, 502–507 (2007). doi:10.1126/science.1139994 Medline

25. I. Hernández-Almeida, F. J. Sierro, I. Cacho, J. A. Flores, Impact of suborbital climate changes in the North Atlantic on ice sheet dynamics at the Mid-Pleistocene Transition. *Paleoceanogr. Paleoclimatol.* **27**, PA3214 (2012). doi:10.1029/2011PA002209

26. R. N. Drysdale, J. C. Hellstrom, G. Zanchetta, A. E. Fallick, M. F. Sánchez Goñi, I. Couchoud, J. McDonald, R. Maas, G. Lohmann, I. Isola, Evidence for obliquity forcing of glacial Termination II. *Science* **325**, 1527–1531 (2009). doi:10.1126/science.1170371 Medline

27. G. Marino, E. J. Rohling, L. Rodríguez-Sanz, K. M. Grant, D. Heslop, A. P. Roberts, J. D. Stanford, J. Yu, Bipolar seesaw control on last interglacial sea level. *Nature* **522**, 197–201 (2015). doi:10.1038/nature14499 Medline

28. B. Martrat, J. O. Grimalt, C. Lopez-Martinez, I. Cacho, F. J. Sierro, J. A. Flores, R. Zahn, M. Canals, J. H. Curtis, D. A. Hodell, Abrupt temperature changes in the Western Mediterranean over the past 250,000 years. *Science* **306**, 1762–1765 (2004). doi:10.1126/science.1101706 Medline

29. B. Martrat, P. Jimenez-Amat, R. Zahn, J. O. Grimalt, Similarities and dissimilarities between the last two deglaciations and interglaciations in the North Atlantic region. *Quat. Sci. Rev.* **99**, 122–134 (2014). doi:10.1016/j.quascirev.2014.06.016

30. D. Hodell, L. Lourens, S. Crowhurst, T. Konijnendijk, R. Tjallingii, F. Jiménez-Espejo, L. Skinner, P. C. Tzedakis, F. Abrantes, G. D. Acton, C. A. Alvarez Zarikian, A. Bahr, B. Balestra, E. L. Barranco, G. Carrara, E. Ducassou, R. D. Flood, J.-A. Flores, S. Furota, J.

Grimalt, P. Grunert, J. Hernández-Molina, J. K. Kim, L. A. Krissek, J. Kuroda, B. Li, J. Lofi, V. Margari, B. Martrat, M. D. Miller, F. Nanayama, N. Nishida, C. Richter, T. Rodrigues, F. J. Rodríguez-Tovar, A. C. F. Roque, M. F. Sanchez Goñi, F. J. Sierro Sánchez, A. D. Singh, C. R. Sloss, D. A. V. Stow, Y. Takashimizu, A. Tzanova, A. Voelker, C. Xuan, T. Williams, A reference time scale for Site U1385 (Shackleton Site) on the SW Iberian Margin. *Global Planet. Change* **133**, 49–64 (2015). doi:10.1016/j.gloplacha.2015.07.002

31. T. Rodrigues, M. Alonso-García, D. A. Hodell, M. Rufino, F. Naughton, J. O. Grimalt, A. H. L. Voelker, F. Abrantes, A 1-Ma record of sea surface temperature and extreme cooling events in the North Atlantic: A perspective from the Iberian Margin. *Quat. Sci. Rev.* **172**, 118–130 (2017). doi:10.1016/j.quascirev.2017.07.004
32. L. Piccini, G. Zanchetta, R. N. Drysdale, J. Hellstrom, I. Isola, A. E. Fallick, G. Leone, M. Doveri, M. Mussi, F. Mantelli, G. Molli, L. Lotti, A. Roncioni, E. Regattieri, M. Meccheri, L. Vaselli, The environmental features of the Monte Corchia cave system (Apuan Alps, central Italy) and their effects on speleothem growth. *Int. J. Speleol.* **37**, 153–172 (2008). doi:10.5038/1827-806X.37.3.2
33. R. N. Drysdale, B. T. Paul, J. C. Hellstrom, I. Couchoud, A. Greig, P. Bajo, G. Zanchetta, I. Isola, C. Spötl, I. Baneschi, E. Regattieri, J. D. Woodhead, Precise microsampling of poorly laminated speleothems for U-series dating. *Quat. Geochronol.* **14**, 38–47 (2012). doi:10.1016/j.quageo.2012.06.009
34. R. N. Drysdale, G. Zanchetta, I. Baneschi, M. Guidi, I. Isola, I. Couchoud, L. Piccini, A. Greig, H. Wong, J. D. Woodhead, E. Regattieri, E. Corrick, B. Paul, C. Spötl, E. Denson, J. Gordon, S. Jaillet, F. Dux, J. C. Hellstrom, Partitioning of Mg, Sr, Ba and U into a subaqueous calcite speleothem. *Geochim. Cosmochim. Acta* **264**, 67–91 (2019). doi:10.1016/j.gca.2019.08.001
35. C. Spötl, T. W. Vennemann, Continuous-flow isotope ratio mass spectrometric analysis of carbonate minerals. *Rapid Commun. Mass Spectrom.* **17**, 1004–1006 (2003). doi:10.1002/rcm.1010 Medline
36. C. Spötl, Long-term performance of the Gasbench isotope ratio mass spectrometry system for the stable isotope analysis of carbonate microsamples. *Rapid Commun. Mass Spectrom.* **25**, 1683–1685 (2011). doi:10.1002/rcm.5037 Medline
37. M. D. Schmitz, B. Schoene, Derivation of isotope ratios, errors, and error correlations for U-Pb geochronology using ^{205}Pb-^{235}U-(^{233}U)-spiked isotope dilution thermal ionization mass spectrometric data. *Geochem. Geophys. Geosyst.* **8**, Q08006 (2007). doi:10.1029/2006GC001492
38. D. A. Richards, S. H. Bottrell, R. A. Cliff, K. Strohle, P. J. Rowe, U-Pb dating of a speleothem of Quaternary age. *Geochim. Cosmochim. Acta* **62**, 3683–3688 (1998). doi:10.1016/S0016-7037(98)00256-7
39. D. A. Richards, J. A. Dorale, Uranium-series chronology and environmental applications of speleothems. *Rev. Mineral. Geochem.* **52**, 407–460 (2003). doi:10.2113/0520407
40. J. Hellstrom, Rapid and accurate U/Th dating using parallel ion-counting multi-collector ICP-MS. *J. Anal. At. Spectrom.* **18**, 1346–1351 (2003). doi:10.1039/b308781f
41. E. J. Hendy, P. J. Tomiak, M. J. Collins, J. Hellstrom, A. W. Tudhope, J. M. Lough, K. E. H. Penkman, Assessing amino acid racemization variability in coral intra-crystalline protein for

geochronological applications. *Geochim. Cosmochim. Acta* **86**, 338–353 (2012). doi:10.1016/j.gca.2012.02.020 Medline

42. D. Scholz, D. Hoffmann, J. C. Hellstrom, C. Bronk Ramsey, A comparison of different methods for speleothem age modelling. *Quat. Geochronol.* **14**, 94–104 (2012). doi:10.1016/j.quageo.2012.03.015

43. R. N. Drysdale, G. Zanchetta, J. C. Hellstrom, A. E. Fallick, J. X. Zhao, Stalagmite evidence for the onset of the last Interglacial in southern Europe at 129 ka. *Geophys. Res. Lett.* **32**, L24708 (2005). doi:10.1029/2005GL024658

44. J. Hellstrom, U-Th dating of speleothems with high initial ^{230}Th using stratigraphical constraint. *Quat. Geochronol.* **1**, 289–295 (2006). doi:10.1016/j.quageo.2007.01.004

45. A. H. L. Voelker, E. Salgueiro, T. Rodrigues, F. J. Jimenez-Espejo, A. Bahr, A. Alberto, I. Loureiro, M. Padilha, A. Rebotim, U. Röhl, Mediterranean Outflow and surface water variability off southern Portugal during the early Pleistocene: A snapshot at Marine Isotope Stages 29 to 34 (1020–1135 ka). *Global Planet. Change* **133**, 223–237 (2015). doi:10.1016/j.gloplacha.2015.08.015

46. A. H. L. Voelker, A. Colman, G. Olack, J. J. Waniek, D. Hodell, Oxygen and hydrogen isotope signatures of Northeast Atlantic water masses. *Deep-Sea Res. Part II* **116**, 89–106 (2015). doi:10.1016/j.dsr2.2014.11.006

47. A. H. L. Voelker, F. J. Jimenez-Espejo, A. Bahr, A. Rebotim, C. Cavaleiro, E. Salgueiro, U. Röhl, Data report: IODP Site U1387: the revised splice between Sections U1387B-18X-3 and U1387C-8R-3 (>171.6 mcd). *Proc. Integr. Ocean Drill. Program* **339**, 1–11 (2018). doi:10.2204/iodp.proc.339.204.2018

48. J. Villanueva, J. O. Grimalt, E. Cortijo, L. Vidal, L. Labeyrie, A biomarker approach to the organic matter deposited in the North Atlantic during the last climatic cycle. *Geochim. Cosmochim. Acta* **61**, 4633–4646 (1997). doi:10.1016/S0016-7037(97)83123-7

49. T. Rodrigues, A. H. L. Voelker, J. O. Grimalt, F. Abrantes, F. Naughton, Iberian Margin sea surface temperature during MIS 15 to 9 (580-300 ka): Glacial suborbital variability versus interglacial stability. *Paleoceanogr. Paleoclimatol.* **26**, PA1204 (2011). doi:10.1029/2010PA001927

50. P. J. Müller, G. Kirst, G. Ruhland, I. von Storch, A. Rosell-Melé, Calibration of the alkenone paleotemperature index $U_{37}^{K'}$ based on core-tops from the eastern South Atlantic and the global ocean (60°N-60°S). *Geochim. Cosmochim. Acta* **62**, 1757–1772 (1998). doi:10.1016/S0016-7037(98)00097-0

51. F. Prahl, S. G. Wakeham, Calibration of unsaturation patterns in long-chain ketones compositions for palaeotemperature assessment. *Nature* **330**, 367–369 (1987). doi:10.1038/330367a0

52. R. N. Drysdale, G. Zanchetta, J. C. Hellstrom, A. E. Fallick, J. McDonald, I. Cartwright, Stalagmite evidence for the precise timing of North Atlantic cold events during the early last glacial. *Geology* **35**, 77–80 (2007). doi:10.1130/G23161A.1

53. W. Dansgaard, The O^{18}-abundance in fresh water. *Geochim. Cosmochim. Acta* **6**, 241–260 (1954). doi:10.1016/0016-7037(54)90003-4

54. J. Zhu, Z. Liu, E. C. Brady, B. L. Otto-Bliesner, S. A. Marcott, J. Zhang, X. Wang, J. Nusbaumer, T. E. Wong, A. Jahn, D. Noone, Investigating the direct meltwater effect in terrestrial oxygen-isotope paleoclimate records using an isotope-enabled Earth system model.

Geophys. Res. Lett. **44**, 12501–12510 (2017). doi:10.1002/2017GL076253

55. D. Paillard, L. Labeyrie, P. Yiou, Macintosh program performs time-series analysis. *Eos* **77**, 379 (1996). doi:10.1029/96EO00259

56. M. Blaauw, A. J. Christen, Flexible paleoclimate age-depth models using an autoregressive gamma process. *Bayesian Anal.* **6**, 457 (2011).

57. L. C. Skinner, C. Waelbroeck, A. E. Scrivner, S. J. Fallon, Radiocarbon evidence for alternating northern and southern sources of ventilation of the deep Atlantic carbon pool during the last deglaciation. *Proc. Natl. Acad. Sci. U.S.A.* **111**, 5480–5484 (2014). doi:10.1073/pnas.1400668111 Medline

58. Past Interglacials Working Group of PAGES, Interglacials of the last 800,000 years. *Rev. Geophys.* **54**, 162–219 (2016). doi:10.1002/2015RG000482

59. G. H. Denton, R. F. Anderson, J. R. Toggweiler, R. L. Edwards, J. M. Schaefer, A. E. Putnam, The last glacial termination. *Science* **328**, 1652–1656 (2010). doi:10.1126/science.1184119 Medline

60. H. Zhang, M. L. Griffiths, J. C. H. Chiang, W. Kong, S. Wu, A. Atwood, J. Huang, H. Cheng, Y. Ning, S. Xie, East Asian hydroclimate modulated by the position of the westerlies during Termination I. *Science* **362**, 580–583 (2018). doi:10.1126/science.aat9393 Medline

61. J. F. McManus, D. W. Oppo, J. L. Cullen, A 0.5-million-year record of millennial-scale climate variability in the North Atlantic. *Science* **283**, 971–975 (1999). doi:10.1126/science.283.5404.971 Medline

62. M. Alonso-Garcia, F. J. Sierro, M. Kucera, J. A. Flores, I. Cacho, N. Andersen, Ocean circulation, ice sheet growth and interhemispheric coupling of millennial climate variability during the mid-Pleistocene (ca 800-400 ka). *Quat. Sci. Rev.* **30**, 3234–3247 (2011). doi:10.1016/j.quascirev.2011.08.005

63. K. Lambeck, H. Rouby, A. Purcell, Y. Sun, M. Sambridge, Sea level and global ice volumes from the Last Glacial Maximum to the Holocene. *Proc. Natl. Acad. Sci. U.S.A.* **111**, 15296–15303 (2014). doi:10.1073/pnas.1411762111 Medline

64. L. Menviel, E. Capron, A. Govin, A. Dutton, L. Tarasov, A. Abe-Ouchi, R. N. Drysdale, P. L. Gibbard, L. Gregoire, F. He, R. F. Ivanovic, M. Kageyama, K. Kawamura, A. Landais, B. L. Otto-Bliesner, I. Oyabu, P. C. Tzedakis, E. Wolff, X. Zhang, The penultimate deglaciation: Protocol for Paleoclimate Modelling Intercomparison Project (PMIP) phase 4 transient numerical simulations between 140 and 127 ka, version 1.0. *Geosci. Model Dev.* **12**, 3649–3685 (2019). doi:10.5194/gmd-12-3649-2019

65. K. R. Ludwig, “User’s Manual for Isoplot/Ex rev. 2.49. A geochronological toolkit for Microsoft Excel” (Berkeley Geochronology Center Special Publication, 2001).

66. S. Barker, G. Knorr, R. L. Edwards, F. Parrenin, A. E. Putnam, L. C. Skinner, E. Wolff, M. Ziegler, 800,000 years of abrupt climate variability. *Science* **334**, 347–351 (2011). doi:10.1126/science.1203580 Medline

67. J. Imbrie, J. Z. Imbrie, Modeling the climatic response to orbital variations. *Science* **207**, 943–953 (1980). doi:10.1126/science.207.4434.943 Medline